

**PHYSICAL TECHNIQUES IN THE STUDY OF
ART, ARCHAEOLOGY AND
CULTURAL HERITAGE**

Editors

DAVID BRADLEY

*University of Surrey
Department of Physics, Guildford,
GU2 7XH, UK*

DUDLEY CREAGH

*University of Canberra
Faculty of Information Sciences and Engineering
Canberra, ACT 2600, Australia*

VOLUME 1



ELSEVIER

Cover photograph: The pots are part of the Egyptian Collection of the Royal Albert Memorial Museum and Art Gallery, Exeter, UK.

Amsterdam • Boston • Heidelberg • London • New York • Oxford
Paris • San Diego • San Francisco • Singapore • Sydney • Tokyo

Contents

ELSEVIER

Radarweg 29, PO Box 211, 1000 AE Amsterdam, The Netherlands
Linacre House, Jordan Hill, Oxford OX2 8DP, UK
The Boulevard, Langford Lane, Kidlington, Oxford OX5 1GB, UK
84 Theobald's Road, London WC1X 8RR, UK
525 B Street, Suite 1900, San Diego, CA 92101-4495, USA
30 Corporate Drive, Suite 400, Burlington, MA 01803, USA

First edition 2006

Copyright © 2006 Elsevier B.V. All rights reserved

No part of this publication may be reproduced, stored in a retrieval system or transmitted in any form or by any means electronic, mechanical, photocopying, recording or otherwise without the prior written permission of the publisher

Permissions may be sought directly from Elsevier's Science & Technology Rights Department in Oxford, UK: phone (+44) (0) 1865 843830; fax (+44) (0) 1865 853333; Email: permissions@elsevier.com. Alternatively you can submit your request online by visiting the Elsevier web site at <http://elsevier.com/locate/permissions>, and selecting: Obtaining permission to use Elsevier material

Notice

No responsibility is assumed by the publisher for any injury and/or damage to persons or property as a matter of products liability, negligence or otherwise, or from any use or operation of any methods, products, instructions or ideas contained in the material herein. Because of rapid advances in the medical sciences, in particular, independent verification of diagnoses and drug dosages should be made

ISBN-13: 978-0-444-52131-6

ISBN-10: 0-444-52131-3

ISSN: 1871-1731

For information on all Elsevier publications
visit our website at books.elsevier.com

Printed and bound in The Netherlands

06 07 08 09 10 10 9 8 7 6 5 4 3 2 1

Working together to grow
libraries in developing countries

www.elsevier.com | www.bookaid.org | www.sabre.org

ELSEVIER

BOOK AID
International

Sabre Foundation

Preface

vii

Chapter 1 The Modern Museum

Jean Louis Boutaine

1. Introduction	3
2. Examination, characterisation, analysis of cultural heritage artefacts ... why?	4
3. Institutions and networks active at the interface between "science and technology" and "cultural heritage"	7
4. Main techniques used in the study of cultural heritage artefacts	11
5. Conclusion	26
Acknowledgements	27
Appendix 1: Some national cultural heritage institutions	27
Appendix 2: Websites of interest in the domain "science and technology" and "cultural heritage"	28
Appendix 3: Some publications of interest in the domain "science and technology" and "cultural heritage"	29
Appendix 4: Questions to be solved by radiography, some examples	29
References	31

Chapter 2 X-ray and Neutron Digital Radiography and Computed Tomography for Cultural Heritage

41

Franco Casali

1. Introduction	43
2. Radiation sources	44
3. Interaction of the radiation with matter	52
4. Digital imaging for X- and γ rays	55
5. Detectors for X- and γ rays	68
6. Experimental acquisition of digital radiographs: some examples	74
7. Digital imaging for neutron radiation	80
8. Computed tomography using X-rays and gamma photons	82
9. Experimental acquisition of computed tomographs: some examples	86
10. Suggestions and Conclusions	98

Appendix A: Basic notions concerning Fourier Transforms	99
Appendix B: Modulation Transfer Function	108
Appendix C: Characteristics of some detection systems	116
Acknowledgements	121
References	121
Chapter 3 Investigation of Diagenetic and Postmortem Bone Mineral Change by Small-Angle X-ray Scattering	125
Jennifer C. Hiller and Tim J. Wess	
1. Introduction and context	126
2. Biomolecular preservation	133
3. Microfocus SAXS and two-dimensional mapping	136
4. Detection of burning and cremation	140
5. Conclusions	145
References	146
Chapter 4 The Use of X-ray Scattering to Analyse Parchment Structure and Degradation	151
Craig J. Kennedy and Tim J. Wess	
1. Parchment	152
2. Techniques	157
3. Results	161
4. Surface to surface analysis of parchment cross sections	163
5. Laser cleaned parchment	166
6. Conclusions	169
References	169
Chapter 5 Egyptian Eye Cosmetics (“Kohls”): Past and Present	173
Andrew D. Hardy, R.I. Walton, R. Vaishnav, K.A. Myers and M.R. Power and D. Pirrie	
1. Introduction	174
2. Materials and methods	180
3. Results	183
4. Discussion	192
5. Conclusions	199
Acknowledgements	201
References	202
Author Index	205
Subject Index	217

Preface

This volume is the first of a series on “Physical Techniques in the Study of Art, Archaeology and Cultural Heritage”. It follows a successful earlier publication by Elsevier (*Radiation in Art and Archaeometry*), also produced by the editors of this book, Dr David Bradley (Department of Physics, University of Surrey) and Professor Dudley Creagh (Director of the Cultural Heritage Research Centre, University of Canberra).

There has been an upsurge of interest world wide in cultural heritage issues, and in particular, large organizations such as UNESCO and the European Union are active in providing funding for a very diverse range of projects in cultural heritage preservation. It is perceived that it is essential to preserve the cultural heritage of societies, both to benefit the future generations of those societies, and to inform other cultures. Also, institutions and locations of cultural heritage significance provide an impetus for the tourist industry of a country, and for many, cultural tourism contributes substantially to their national economy.

A growing need exists for the education of conservators and restorers because it is these professionals who will make decisions on how best to preserve our cultural heritage. Therefore, the primary aim of this book series is the dissemination of technical information on scientific conservation to scientific conservators, museum curators, conservation science students, and other interested people.

Scientific conservation, as a discipline, is a comparatively modern concept. For many years, interested scientists have addressed scientific problems associated with cultural heritage artefacts. But their involvement has been sporadic and driven by the needs of individual museums, rather than a personal lifetime study of issues of conservation of, for example, buildings, large functional objects, paintings, and so on.

The contributors of this book series are from both “interested scientists” and the “museum-based scientists”. The authors have been selected with an eye to involving young as well as established scientists.

The author of chapter 1, Dr Jean Louis Boutaine, was Head of the Research Department of the *Centre de Recherche et de Restauration des Musées de France* at the Louvre, at his retirement. He trained initially as a physicist in the application of non-destructive analytical techniques, and has extensive experience in equipment design, and in the application of radioisotopes to the solution of scientific problems. Dr Boutaine has had the most distinguished career within the conservation science community. Since his retirement, he has been extremely active in driving the expansion of cultural heritage research within the European Community, through involvement in EU Projects and the organization of

conferences; He is the EU-ARTECH Networking Activity Coordinator. This chapter is a veritable “treasure trove” of information. It discusses the use of science and technology to study aspects of the preservation of cultural heritage taken in its broadest sense: works of art, museum collections, books, manuscripts, drawings, archival documents, musical instruments, ethnographic objects, archaeological findings, natural history collections, historical buildings, industrial heritage objects and building. This chapter explains how science and technology are used to provide information which will assist us to understand how the artefacts have been created, how they have been handled (or mis-handled) since their creation, and how we can preserve them for the culture and the pleasure of future generations.

A review of the different techniques (examination, characterization, analysis) which are applied in this discipline of “conservation science” is presented. This is illustrated by many recent examples in various cultural areas. Some major national cultural heritage institutions, as well as European networks active in this area, are indicated. An important bibliography, including websites of interest, is provided.

The author of chapter 2, Professor Franco Casali, is a physicist by training and his interests include the study of scientific conservation. He has been a researcher at the ENEA (the Italian nuclear authority) and was the Director of a Research Centre with two experimental reactors. He was also an Expert of the United Nations (IAEA) for nuclear power stations. His last position at the ENEA was as Director of Physics and Scientific Calculus Division of the ENEA. Since 1985, he has been associated with “Health Physics” at the University of Bologna. Also, he is responsible for the teaching of “Archaeometry”. At the University of Bologna, he leads a group of young physicists and computer science experts, who have developed advanced equipment for both micro-Computer Tomography and for large-object Computer Tomography. He has been one of the Italian representatives in the European Neutron Radiography Working Group.

This chapter commences with a description of the physical principles underlying the techniques of X-ray and neutron and digital radiography. It then proceeds to discuss the application of these techniques for the study of objects of cultural heritage significance.

Professor Tim Wess is responsible for Chapters 3 and 4 of this volume, which were co-authored by his research associates (Jennifer Hiller, in Chapter 3, and Craig Kennedy, in Chapter 4). Professor Wess holds the Chair of Biomaterials in the Biophysics Division in the School of Optometry and Vision Science at Cardiff University. His research interests include: the characterization of partially ordered biopolymers and mineralizing systems; and structural alterations of biophysical systems due to strain and /or degradation. The systems in which he is interested contain collagen, fibrillin, and cellulose (which relate, in the cultural heritage discipline, to an interest in parchment and papers). A parallel interest is in the structure of bone and artificial composite materials (which relates to his interest in historical studies of bone materials).

Chapter 3 will describe the technique of SAXS (Small-angle X-ray scattering), and show how this has been used to study alteration to structure of minerals in the bone. Preservation of intact bone mineral crystallites has been shown to relate to the endurance of amplifiable ancient DNA from archaeological and fossil bone. Moreover, the variation in bone crystallite size and habit across a two-dimensional area has been studied in modern and archaeological samples. Finally, the alteration to bone mineral during experimental heating has been investigated.

In Chapter 4, there is a description of research being undertaken on historical parchments in collaboration with Dr K. Nielsen and Rene Larsen (School of Conservation, Copenhagen, Denmark). This research involves the analysis of the deterioration of historic parchments and also the simulation of the ageing process by induced oxidative damage. (This work has been supported by the EU 5th Framework on Cultural Heritage Conservation and the National Archive for Scotland).

The author of chapter 5, Andrew Hardy, received his D.Phil. in X-ray Crystallography, from Sussex University (UK) in 1971. He began studying Middle Eastern eye cosmetics (“kohls”) in the early 1990s whilst working in Oman. He has continued this work in his present position at the School of Humanities and Social Sciences, Exeter University, Political and Sociological Studies, Exeter University. The chapter summarizes and reviews the published data on the usage and composition of kohls in ancient (Pharaonic) Egypt. It also gives some information, from later time periods, on kohl usage and its “recipes”. This is followed by a brief description of the experimental techniques used in his studies of past and present Egyptian kohl samples. The techniques used were: XRPD (X-ray powder diffraction), LV SEM (low vacuum scanning electron microscopy), IR (infrared spectroscopy) and the relatively new technique QEMSCAN (quantitative scanning electron microscopy). Results are given on thirty-three samples of both old and new kohls using these analytical techniques. The old samples were obtained from the Pharaonic kohl pots shown on the front cover of this book; the pots are part of the Egyptian collection of the Royal Albert Memorial Museum and Art Gallery, Exeter, UK. Finally, there is a comparison of past and present kohl compositions, concentrating on the toxicology of lead and how it is related to the particle size of the galena present. Also, there is consideration of the cultural usage of kohl, via information on its containers etc., in ancient and modern-day Egypt.

Chapter 2

X-ray and Neutron Digital Radiography and Computed Tomography for Cultural Heritage

Franco Casali

*Department of Physics, University of Bologna, Italy
Email: franco.casali@bo.infn.it
www.xraytomography.com*

Abstract

Methods of diagnosis based on digital radiography (DR) and computed tomography (CT), are more and more frequently used in the cultural heritage field. The application of these techniques can help restoration and conservation planners to understand historical construction techniques and to reveal poor restoration work and forgeries.

As the size of objects of cultural interest varies greatly, from small fragments (for which high spatial resolution is needed) to large works of art (for which large detectors are necessary), it would not be appropriate to describe any one particular measuring device in detail. In this chapter, we will therefore provide an overview on Digital Radiography (DR) and Computed Tomography (CT) systems, underlining their range of applications. The chapter focuses mainly on X-ray radiation (with different kinds of sources) although neutron DR and CT are also mentioned, as neutron imaging should be considered complementary to X-ray imaging.

Some DR and CT images, most of which were taken by researchers at the Department of Physics of the University of Bologna, are shown. This overview adopts a tutorial approach, as it is aimed at those with no specific knowledge of digital imaging. Three appendices have also been included (concerning Fourier transforms, modulation transfer function and DR and CT acquisition systems) for those readers who wish to acquire further skills in the field of digital imaging.

Keywords: X-ray digital radiography, tomography, neutron imaging, neutron CT, cultural heritage digital imaging.

Contents

1. Introduction	43
1.1. Electromagnetic radiation for internal investigations	43
1.2. Particle beams	44
1.3. Ultrasound and Sonic waves	44
2. Radiation sources	44
2.1. X-rays and γ rays	44
2.1.1. What are X-rays?	44
2.1.2. What are γ rays?	47
2.2. Neutrons	48
2.3. X-ray sources	48
2.3.1. X-ray tubes	48
2.3.2. Linear accelerators (LINAC)	50
2.3.3. Synchrotrons	51
2.4. Radioisotope sources	51

3. Interaction of the radiation with matter	52
3.1. General considerations	52
3.2. Good geometry	53
3.3. "Beam hardening" for photons	54
4. Digital imaging for X- and γ rays	55
4.1. General considerations	55
4.2. Image digitising	56
4.2.1. Foreword	56
4.2.2. The "sampling theorem" for spatial reproduction	57
4.2.3. Discretising the grey interval	57
4.3. Image enhancement	59
4.3.1. The histogram of a digital image	59
4.3.2. Contrast enhancement	62
4.3.3. Segmentation	64
4.3.4. Frame summing	64
4.3.5. Pixel binning	66
4.4. Spatial filters	66
4.4.1. Introduction	66
4.4.2. Image enhancement in the spatial domain	67
4.4.3. Fourier-Transform-based filtering	68
5. Detectors for X- and γ Rays	68
5.1. Families of detectors	68
5.2. Geometry of the detection systems	69
5.2.1. Single detector (point geometry)	69
5.2.2. Linear geometry (linear array)	70
5.2.3. Bidimensional geometry (planar detector)	71
5.3. The Modulation Transfer Function (MTF)	71
6. Experimental acquisition of digital radiographs: some examples	74
6.1. Acquisition by linear arrays	74
6.2. Acquisition using planar detectors	76
6.3. The advantages and disadvantages of digitising	78
7. Digital imaging for neutron radiation	80
7.1. General considerations	80
7.2. Planar detectors for neutrons	81
8. Computed tomography using X-rays and gamma photons	82
8.1. General considerations	82
8.2. Types of computed tomography systems	82
8.2.1. First generation CT system	82
8.2.2. Second generation CT system	84
8.2.3. Third generation CT system	84
8.2.4. Medical CT	85
8.2.5. "Cone beam" tomography	85
9. Experimental acquisition of computed tomographs: some examples	86
9.1. Foreword	86
9.2. Microtomography	86
9.2.1. Microtomography in cone beam geometry	86
9.2.2. Microtomography with a linear detector	86
9.3. Medium-size CT systems	87
9.3.1. CT system with EBCCD	87
9.3.2. Medium-high energy	89
9.4. Computed tomography of a large ancient globe	91
9.5. Neutron tomography	97
9.6. Induced activation by X-rays and neutrons	97
9.6.1. Activation by X-rays	97
9.6.2. Activation by neutrons	98

X-ray and Neutron Digital Radiography and Computed Tomography	43
10. Suggestions and conclusions	98
Appendix A: Basic notions concerning Fourier transforms	99
A.1. The Fourier series	99
A.2. One-dimensional Fourier transform	101
A.3. Two-dimensional Fourier transform	102
A.4. One-dimensional discrete Fourier transform	103
A.5. Two-dimensional discrete Fourier transform	103
A.6. Some properties of 2D discrete Fourier transforms	104
Mean value	104
Periodicity and symmetry	105
A.7. Filtering in the frequency domain	106
A.8 Convolution of two functions	107
Convolution Theorem	107
Appendix B: Modulation Transfer Function	108
B.1. Point spread function, line spread function and edge spread function	108
B.2. Optical Transfer Function and Modulation Transfer Function	113
Introduction	113
B.3. Measurement of the Modulation Transfer Function for a linear system	113
B.4. Modulation Transfer Function: general definition	114
Appendix C: Characteristics of some detection systems	116
C.1. General considerations	116
C.2. Flat panels	116
C.3. CCD-based systems	117
Scintillating screen	118
CCD camera	120
Acknowledgements	121
References	121

1. INTRODUCTION

Physical methods of diagnosis are finding more and more applications in the cultural heritage field either for scientific investigation or for restoration and conservation purposes. It is often vitally important to gain information on the invisible parts of a work of art or archaeological find, revealing the artist's preparatory sketch or changes of idea or for example, to examine the state of corrosion of a bronze statue or the cracks in a marble statue. For additional information, please refer to Chapter 1. These diagnostic techniques refer primarily to the investigations performed using electromagnetic radiation at various wavelengths, particle beams and sound waves. These techniques must be as non-invasive as possible.

1.1. Electromagnetic radiation for internal investigations

Several potential applications exist, depending on the wavelength of the electromagnetic radiation:

- wavelength of approximately 10 mm (georadar); (in the cultural heritage field, this technique is used for detecting old foundations, empty rooms, invisible galleries and so on);
- wavelength of approximately 1000–3000 nm (infrared) (useful for detecting preparatory sketches hidden below layers of paint);
- wavelength of less than 5 nm for X-rays and less than 0.1 nm for gamma rays (used for performing radiographs and tomographs).

1.2. Particle beams

In the cultural heritage field, neutrons are most frequently used for conducting internal investigations and they have complementary characteristics to those of X-rays and gamma rays. For “surface” or “shallow” investigations, electrons (SEM-TEM) and alpha particles and protons (particle induced X-ray emission = PIXE) can also be used.

1.3. Ultrasound and Sonic waves

Sonic waves and ultrasound techniques are mechanical weak impact stresses useful in cases where X-rays have low penetration.

- Sonic waves provide useful information on the interior of brick-built columns or columns built using non-homogeneous materials.
- Ultrasound provides information on cracks or discontinuities in metals or stone objects (*e.g.* columns), where the X-rays are not suitable given the thickness of the object being examined.

Generally speaking, a diagnostic imaging system consists of:

- a radiation source;
- a radiation detector;
- equipment for moving the object in relation to the source-detector loading;
- a computer for managing the image acquisition process;
- a computer for image processing and rendering.

In this chapter, some basic elements on digital radiography (DR) and computed tomography (CT) will be given, relating primarily to X- and γ rays (and, to a lesser extent, neutrons). Even if DR is the natural extension of radiography, there is an increasing interest in CT. In fact, this kind of diagnosis gives more information than DR as it is apparent from Figs. 1 to 3.

Figure 1 reproduces the image of a small clay bust, a copy of one found at Pompeii (this image will be our reference for subsequent elaborations). Figure 2 reproduces some radiographies of this small bust and Fig. 3 gives the 3D representation of it after a CT. A small defect, of the order of 800 μm not visible by DR, is clearly detectable by CT (Fig. 3 – right).

This overview is addressed mainly to people working in the field of cultural heritage like restorers, conservators and art critics.

2. RADIATION SOURCES

2.1. X-rays and γ rays

2.1.1. What are X-rays?

The X- and γ rays are produced by “photons”, electromagnetic wave packets that can behave either as waves or particles. Photons are characterised by their wavelength, λ , and



Fig. 1. Photo of a small clay head, copy of a find from Pompeii.



Fig. 2. X-ray radiographies of the object in Fig. 1.

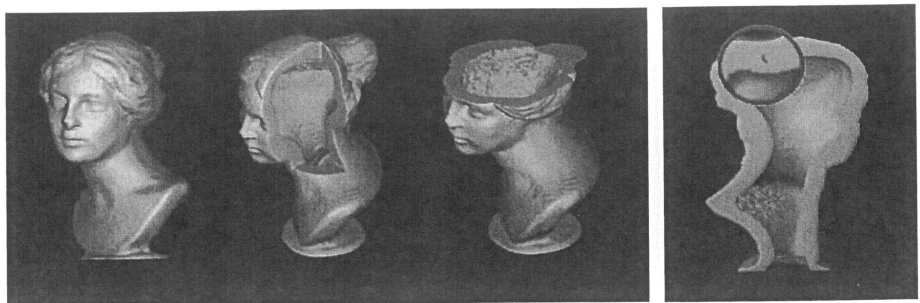


Fig. 3. Three-dimensional representation of the 3D CT image of the object in Fig. 1 (left) and a small defect in the clay (about 0.8 mm), not visible on X-ray radiography (right).

energy, E . These two quantities are related by the following expression:

$$E = h\nu = hc/\lambda \quad (1)$$

where:

h = Planck constant;

ν = frequency;

c = light speed.

The wave aspect of photons appears mainly at low frequencies (*e.g.* radio or TV waves), the particle aspect is predominant for high frequencies (high energy). For the applications in question, we can consider that photons act as particles.

The X-ray photons of interest to us have energies ranging from a few keV to several MeV (far more energetic than the visible light photons). As the minimum energy required for ionisation is 10 eV (UV radiation), X-rays are considered as “ionising radiation”, and they must be used with care.

X-rays, which were discovered in 1895 by W. Roentgen,¹ can be generated in two ways.

1. When fast electrons undergo acceleration (or deceleration) they emit photons, also known as “bremsstrahlung” radiation. The energy distribution of photons or “energy spectrum” is of the continuous type (“white radiation”);
2. When electrons are removed from the innermost orbits of an atom (see Fig. 4), the electrons, which belong to the outer orbits, jump into the “holes” created. In this process of rearrangement, photons are emitted with energies equivalent to the difference between the binding energies of the inner and outer orbits. In such cases, the energies spectrum of emitted photons is a “line spectrum”. These particular energies (characteristic of each element) are also known as “lines of X-ray fluorescence”. If fast electrons impinge on a material, the resulting X-ray spectrum is the overlap between the continuous and fluorescence spectrum (see Fig. 5).

¹ For his discovery, W. Roentgen received the Nobel Prize for Physics. Roentgen did not accept the prize money; rather he used it to set up fellowships for the best young German physicists.

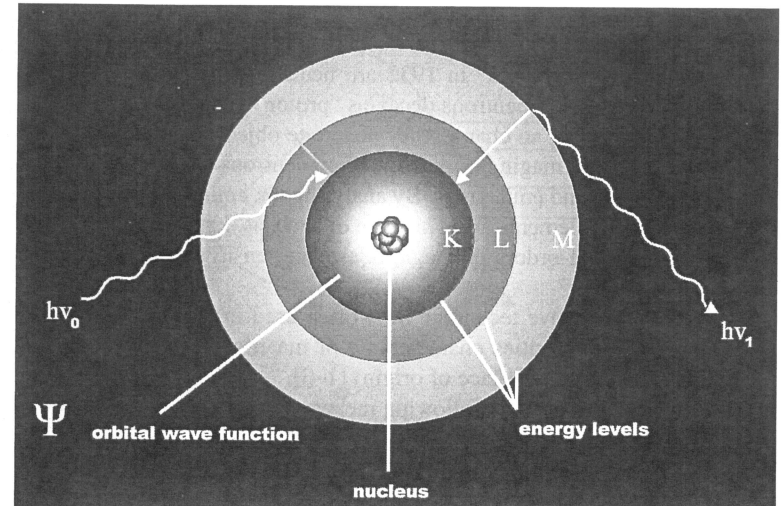


Fig. 4. Diagram of atomic shell structure and interaction with ionising photons.

2.1.2. What are γ rays?

Gamma rays are photons. They cannot be distinguished from X-ray photons since both are electromagnetic radiation. Gamma rays are produced during the reassembly of the nucleus after specific nuclear reactions (*e.g.* α or β decays and the capture of other particles). For particular nuclei and particular reactions, the emitted photons always have the same energy and the γ spectrum is of a “line” type. It is possible to identify the radioactive isotopes from the line distribution in the spectrum.

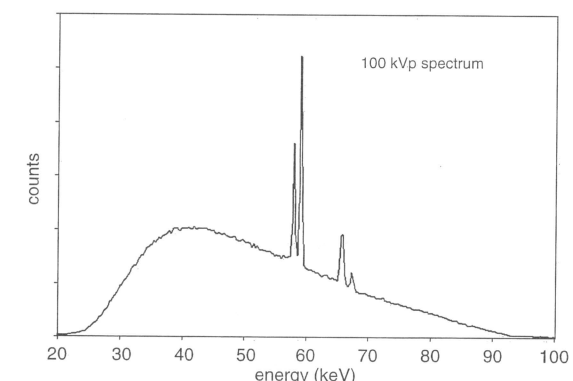


Fig. 5. Radiation spectra of a conventional X-ray tube. The continuous component, due to bremsstrahlung, and the discrete component, due to characteristic emission, are visible.

2.2. Neutrons

Neutrons, discovered by Chadwick² in 1932 are neutral particles that make up part of atomic nuclei. In the free state, neutrons decay as “proton + electron + antineutrino” with a mean life of 1000 s. Having no charge, they penetrate objects easily, which makes them good probes for diagnostic imaging purposes. When neutrons are captured by nuclei, the nuclei become radioactive and emit γ rays. By analysing the emitted spectrum, it is possible to infer what the activated elements are. This type of analysis, known as Neutron Activation Analysis (NAA), is several orders of magnitude more sensitive than standard chemical analysis.

As NAA is a non-destructive technique, it is often used in archaeometry for detecting traces of materials (e.g. impurities characteristic of materials from a certain mine, thus enabling the identification of the place of origin) [1–3].

Neutrons can be produced by the following means:

1. nuclear reactors, through the fission induced in particular isotopes such as U^{235} , U^{238} or Pu^{239} ;
2. spontaneous fissions, for instance Cf^{252} ;
3. particular nuclear reactions making use of particle accelerators (for instance, bombarding Be^9 with α -particles);
4. small accelerators in which the reaction $H^2 + H^3 \rightarrow He^4 + n$ occurs.

2.3. X-ray sources

The X-ray sources of interest in this chapter can be summarised as:

- X-ray tubes (from 5 to 450 kV);
- linear accelerators (from 2 to 15 MV);
- synchrotron light (from 5 to 100 keV).

2.3.1. X-ray tubes

A schematic diagram of a typical X-ray tube is shown in Fig. 6. The electrons, produced by a heated filament inside a glass tube – where high vacuum has been created – are accelerated against a target (anode). For electron energy less than 1 MeV, bremsstrahlung radiation is produced mainly perpendicular to the electrons’ direction of flight; otherwise, for energy higher than 1 MeV, X-ray radiation is mainly produced in a forward direction [4].

Only a small fraction of the kinetic energy of the electrons is transformed into X-rays: the remainder heats the anode. For good anode cooling, a rotating target (or a cooling circuit) is used, mainly for tubes with powers higher than 100 W. When the object being tested is made of heavy material, industrial tubes are used. These are designed to operate continuously; long exposure time (several hours) is normal. On the contrary, medical tubes are designed to give short high power shots, in order to minimise motion artefacts.

² For his discovery, Edwin Chadwick received the Nobel Price for Physics in 1935.

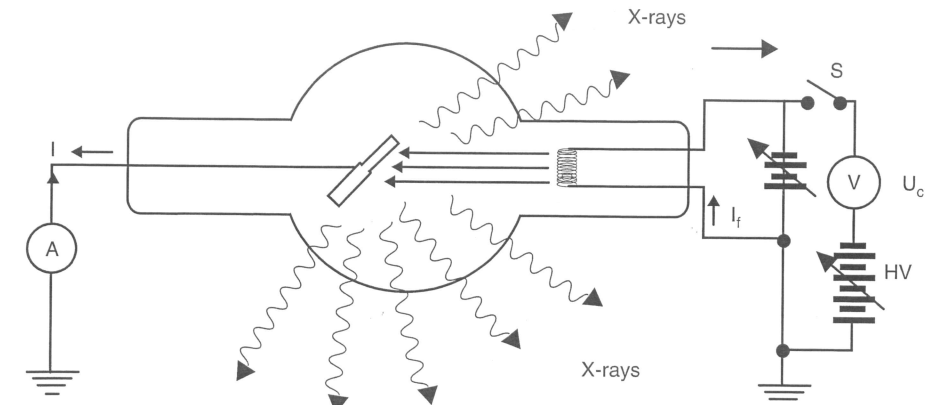


Fig. 6. Diagram of an X-ray tube.

The effective size of the anode from which the X-ray beam is emitted is called the “focal spot”. Focal spot dimension is very important for image definition. The smaller the focal spot, the sharper is the “shadow” produced by the X-ray beam on the detector. For extended focal spots there is a penumbra known as “source unsharpness”, as shown in Fig. 7.

The penumbra dimension can be calculated using the following formula:

$$P = \frac{fD}{d}. \quad (2)$$

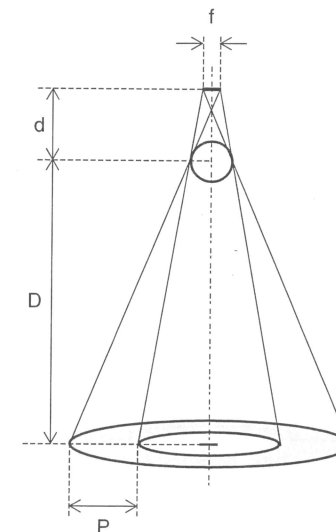


Fig. 7. Unsharpness, due to the real size of the focal spot of an X-ray source.

where:

- P = width of the penumbra;
- f = effective focal spot size;
- D = distance between object and image plane;
- d = distance between source target and object.

Microfocus and Nanofocus Tubes. For having high spatial resolution (low “penumbra”), X-ray tubes, called microfocus tubes, are used where the focal spot is of the order of few microns. X-ray tubes are now available with focal spots that can reach dimensions of 0.5 microns (nanofocus). Because of heat-loading effects in the anode in these (rather expensive) tubes, current is low (a few μA) and maximum voltage does not exceed 150 kV. Using micro-focus, or nanofocus, it is possible to obtain the CT of small objects with high spatial resolution.

Industrial Tubes. For high currents and voltage up to 450 kV, industrial type tubes are used. Usually they have a cooled anode and current can reach several milliamperes. These tubes can be used for radiography or CT of bronze statues of several millimetre thickness. Both microfocusses or industrial tubes operate in a continuous way.

2.3.2. Linear accelerators (LINAC)

Figure 8 shows the scheme of a linear accelerator or LINAC (LINear ACcelerator). The electrons emitted from the cathode are “packaged” and accelerated against the anode by an electromagnetic wave of a suitable frequency (radio frequency), like a surfer carried to the shore by a wave. The derived bremsstrahlung is, therefore, of pulsed type. The pulse frequency can range up to several MHz. The maximum energy of the photons produced is the maximum energy achieved by the electrons; however very few photons have maximum energy. The energy spectrum is continuous (Fig. 9). Without suitable absorbers (filters), one can

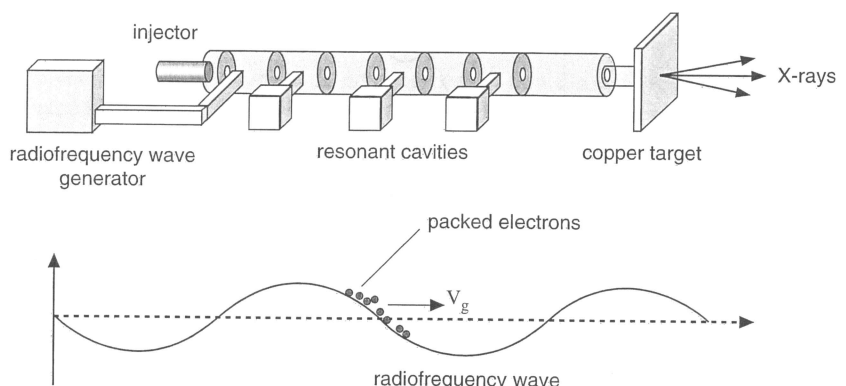


Fig. 8. Schematic representation of a linear accelerator with resonant cavities and a copper target struck by accelerated electrons. High-energy photons are produced by this interaction.

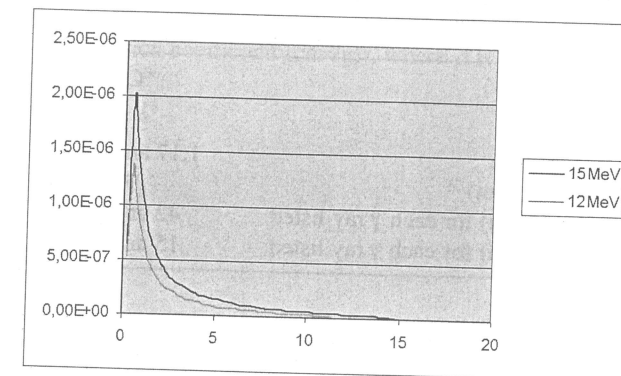


Fig. 9. X-ray spectra produced by a 12 MeV and 15 MeV LINAC (courtesy Dan Schneberk, LLNL).

assume the “effective energy” (equivalent to a monochromatic source) to be one-third of the maximum energy or less.

Linear accelerators can be used for DR or CT of thick or high-density objects (for instance, see Ref. [5]). Portable LINACs do exist, however to the author’s knowledge, they are not yet used “on the field” for cultural heritage applications.

2.3.3. Synchrotrons

Synchrotrons are electron accelerators shaped like a large ring. Electrons can achieve energies of several GeV. If electrons are compelled to move out of their orbit by deflecting magnets or by arrays of bending magnets, they emit an X-ray radiation named “synchrotron light”. This radiation, ranging from 5 to 100 keV, can be selected in energy by proper monochromator crystals, making use of “Bragg’s law”. The synchrotron light is so intense that it is possible to obtain very high energy definition [6–8].

2.4. Radioisotope sources

At present, the radioisotope sources most commonly used in the cultural heritage field for the radiographic analysis of statues and other works have been ^{60}Co and ^{137}Cs , as in the case of the radiographs performed on the arm of Michelangelo’s David [9], the Riace bronzes, a Roman bronze statue [10], and so on.

The *advantages* of using isotopic sources are their low cost (in comparison to the LINAC), the single energy of the emitted photons, and the small dimension of the probes, which enables inspections that would otherwise be impossible.

The *disadvantages* are: the source dimensions (corresponding to a large focal spot), the difficulty of transportation (due to shielding and safety limitations) and handling, and their decrease in intensity (rather low) with time.

Table 1. Important characteristics of two radioisotopic sources (from Ref. [11])

Isotope	^{60}Co	^{137}Cs
Half-life (year)	5.3	30
Gamma ray(s) energy (MeV)	1.17 and 1.33	0.66
Practical source diameter (mm)	3	10
Al half-value thickness* (mm) for each γ ray listed	42 and 48	34
Fe half-value thickness* (mm) for each γ ray listed	15 and 17	12

* The “half-value thickness” is the thickness of a material that reduces the beam intensity to half.

The disintegration intensity decreases exponentially over time:

$$n(t) = n_0 e^{-\lambda t} \quad (3)$$

where:

$n(t)$ = disintegration number at the time t

n_0 = disintegration number at the time $t = 0$, when the intensity of the source is defined

λ = decay rate (disintegration/second).

The quantity λ is related to the half-time, $T^{1/2}$, by the following relation:

$$\lambda = \frac{\ln 2}{T^{1/2}} = \frac{0.693}{T^{1/2}}. \quad (4)$$

The source power, that is the disintegration rate (dis/s), is expressed in “becquerel” (Bq) (one Bq corresponds to one disintegration or transmutation per second). In the past, “curie” (Ci), corresponding to 3.7×10^{10} dis/s, was used as a unit of measurement.

Table 1 gives the characteristics of ^{60}Co and ^{137}Cs , the two commonly used isotopic sources.

3. INTERACTION OF THE RADIATION WITH MATTER

3.1. General considerations

The imaging diagnostic techniques in question (radiography and tomography) concern the attenuation of particle beams through their interaction with matter. We consider both neutrons and photons as particles.

In “good geometry” conditions, for parallel particle beams, the attenuation follows the Beer-Lambert’s Law:

$$I(d) = I_0 e^{-kd} \quad (5)$$

where:

$I(d)$ = the particle number passing through a body with a thickness d ;

I_0 = the particle number which reaches the detector without the body;

k = radiation attenuation coefficient.

For photons, k is indicated by the Greek letter μ (linear attenuation coefficient (cm^{-1})) or by μ/ρ (mass attenuation coefficient (cm^2/g)), where ρ is density (g/cm^3). In this case, equation (5) becomes:

$$I(d) = I_0 e^{-\mu d} \quad (6a)$$

or

$$I(d) = I_0 e^{-(\mu/\rho)d}. \quad (6b)$$

For neutrons, k is indicated by the Greek letter Σ (total macroscopic cross section (cm^{-1})) and equation (5) becomes:

$$I(d) = I_0 e^{-\Sigma d}. \quad (7)$$

Both μ and Σ are rather complicated functions which depend on the irradiated material and particle energy. Figures 10 and 11 show typical shapes of (μ/ρ) and Σ .

3.2. Good geometry

In physical measurements, “good geometry” is used to describe a situation in which a particle, which interacts with the medium under investigation – so that is removed from the beam – does not interact in any other way with the detector. This does not occur when, after one or more shots, the particle is deviated on the detector and is counted as though it has had no interactions with matter. Figure 12 clarifies this concept.

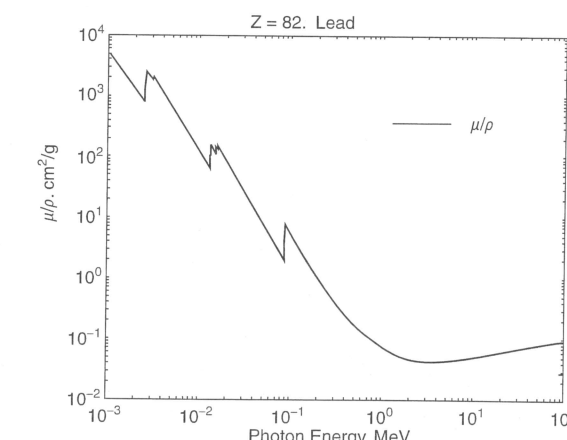


Fig. 10. X-ray mass attenuation coefficient for lead (From Ref. [50]).

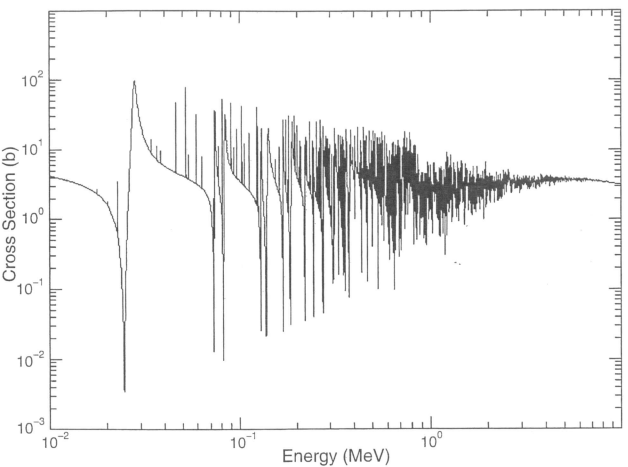


Fig. 11. Neutron microscopic total cross section.

This indirect component is called “diffused radiation”; sometimes in poor-geometry conditions, the diffused radiation is one order of magnitude larger than the direct radiation. Diffused radiation can be eliminated, or decreased, by the use of suitable collimators (see Fig. 13).

3.3. “Beam hardening” for photons

Usually the smaller the energy of interacting particle, the higher will be the attenuation coefficients. When the radiation is not monochromatic (Fig. 5), the weaker component is

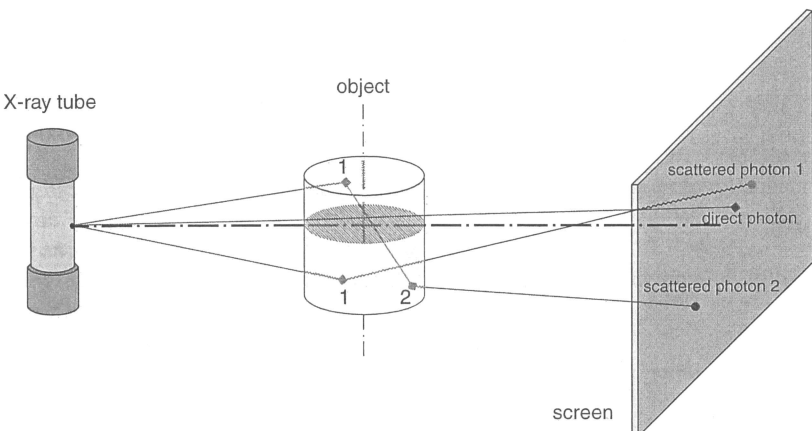


Fig. 12. Interaction of photons (scattered and unscattered) with an object.

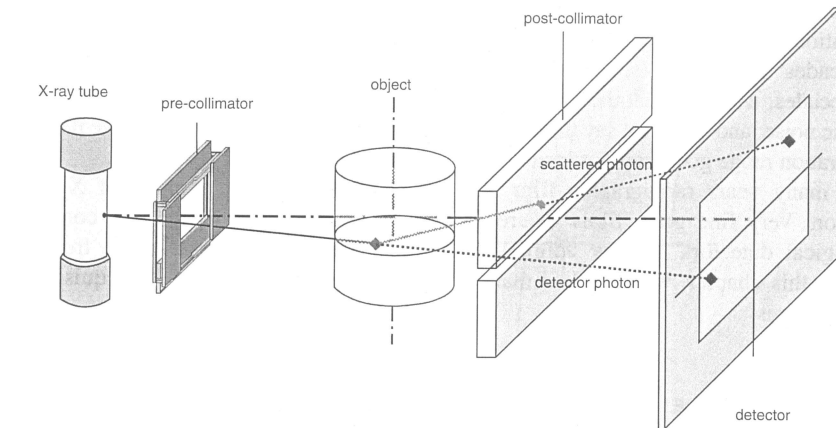


Fig. 13. Pre-collimation and post-collimation of the radiation beam to reduce the scattered component.

absorbed more easily than the harder one; consequentially, when the radiation penetrates deep into the object, the energetic spectrum becomes harder and harder. This phenomenon is called the “beam hardening effect”. In CT, where the absorption coefficient is assumed to be constant with energy, it is necessary to correct this “hardening”, which is equivalent to a variation of μ inside the object, even if it has a homogeneous composition.

4. DIGITAL IMAGING FOR X- AND γ RAYS

4.1. General considerations

In an ideal detection system, a photon, originating from a point source, reaches the detector with a probability given by Beer’s law, expressed by equation (6a). However, a large number of factors render this equation invalid. Firstly, it should be pointed out that the radiation source is not a point (*e.g.* focal spot of finite dimension for X-ray tubes). The second reason is the photon diffusion over the detector during interaction with the object and the experimental fixtures (collimators, room, walls, etc.). The third cause is the photon diffusion inside the detector. The image degradation created by these three causes is known as “blurring”. If N_p is the number of primary photons, which arrive at the detector, and N_s is the number of scattered photons, the ratio (N_p/N_s) can be considered as the ratio between the true signal (N_p) and noise (N_s). A simple increase in primary radiation does not increase the “signal-to-noise-ratio”. This can be achieved using suitable collimators, adjusting the object–screen distance, decreasing the detector thickness, and so on. One very important characteristic of a detection system is the “dynamic range”, defined as the ratio of the maximum and minimum detectable signal. If we consider radiographic film, it suffers from

an intrinsic noise (“fog”) and shows a maximum exposition level beyond which there is “saturation” (all the silver grains are separated from the iodine). The dynamic range is stated in “decades” or in “bits” (see Section 4.2.3). When we say that a film has a dynamic range of 3 decades, we mean that the radiation intensity which gives saturation is 1000 times the intrinsic noise; and when we say that a detector has a dynamic range of 12 bits, we mean that its operation range goes from intrinsic noise to $2^{12} = 4096$ times the background.

For many years radiographic film was the only detector and register of X- and γ radiation. Very fine grain films assure high spatial resolution [12] and are considered “analogue detectors”. Today “digital detectors” (see Section 5) are more frequently used. In this chapter, we will deal mainly with detectors suitable for the acquisition of digital images.

4.2. Image digitising

4.2.1. Foreword

Let us assume a wish to “digitise” an image acquired by a radiographic film. Such an operation can be performed by: (a) taking the film and reading the degree of transparency (related to the “optical density”) by a small detector by moving it step by step and (b) transforming the obtained value into a binary one by means of an Analogue to Digital Converter (ADC).

The “digital” image obtained is a matrix of numbers, similar to a chessboard. The procedure described is commonly used in scanners for transforming “analogue images” (photos or texts) into “digital images”. The smallest matrix element is called a *pixel* (PICTure ELEMENT) (Fig. 14(A)). Therefore, we are in the presence of two types of discretisation: the first concerning spatial sampling, the second, the subdivision of the grey interval (from black to white). A digitising scheme for an analogue signal is given in Fig. 14(B). If we normalise the intensity range, associating the black to zero and the white to one, the problem is how to pass from the continuous grey interval (black \rightarrow white) into a finite number of grey levels.

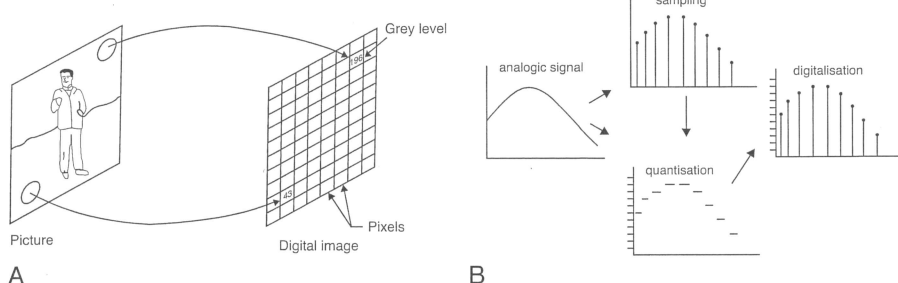


Fig. 14. (A) Image digitising scheme; (B) Analogue signal digitising scheme.

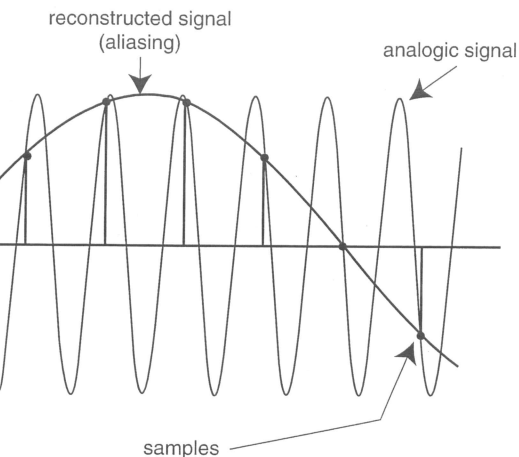


Fig. 15. A periodic signal is sampled with a pitch larger than $\lambda/4$ and the reconstructed signal is different from the original.

4.2.2. The “sampling theorem” for spatial reproduction

Spatial resolution, that is the quality of the reproduction, depends on the “sampling pitch”. A theorem³ (called “Nyquist or Shannon sampling theorem”) says that, unambiguous imaging of a feature of size d is best performed when the sampling pitch is less than $d/2$. Inadequate sampling results in detail loss: in such cases, we obtain so-called “aliasing”⁴. An example of aliasing is shown in Fig. 15. In this example, a periodic signal is sampled with a pitch larger than $\lambda/4$, an amount larger than that allowable by the Nyquist theorem, and the reconstructed signal is totally different (“alias”) from the original one.

Figure 16 reproduces the image of the clay bust represented in Fig. 1, at different sampling pitches (256, 64, 32, 16 dots per inch (dpi)). Obviously many details are lost when a very large sampling pitch is used.

4.2.3. Discretising the grey interval

Having “sampled” the image in space, for each pixel we must allocate a “number” to the grey level. Once again, the quality of the reproduction of the grey tones depends on how many sub-intervals the “black-white” range is subdivided into. For colour images, one has to discretise each primary colour (red, green, blue). If the sub-intervals are too few, e.g. $16 = 2^4$ (ADC at 4 bits), reproduction will be coarse; if the number is high, e.g. $256 = 2^8$ grey levels

³The sampling theorem was stated by Nyquist in 1928 and mathematically proven by Shannon in 1949. This sampling theorem is called “Nyquist Sampling Theorem”, or “Shannon Sampling Theorem” and it is valid in the acoustic field too.

⁴A terrible word obtained declining in English the Latin word “alias”!

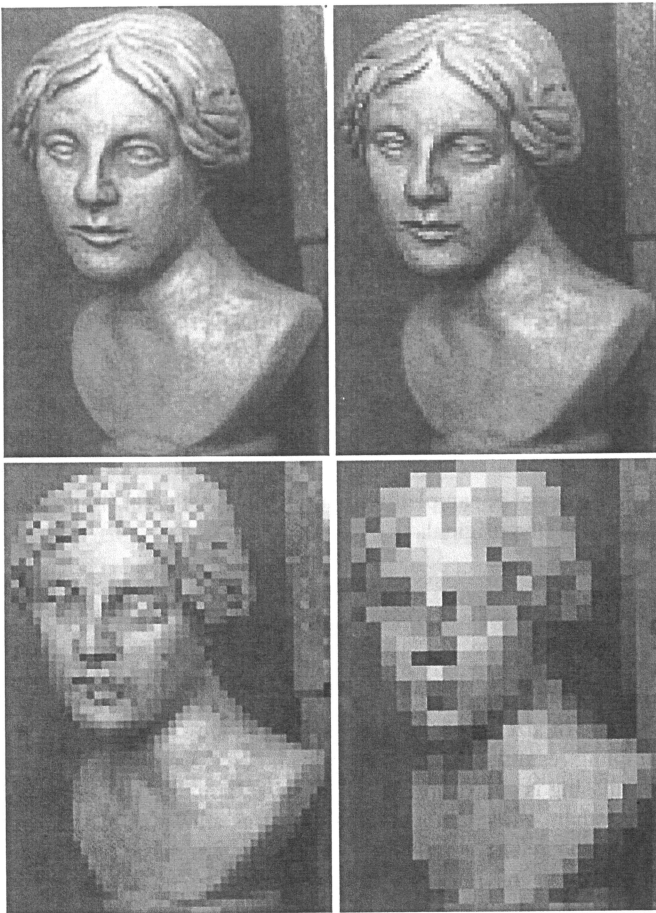


Fig. 16. The test digital image as a function of sampling pitch. The aliasing effect is evident for low pixel numbers (large sampling pitches).

(ADC at 8 bits), reproduction may be acceptable. As the human eye cannot distinguish more than 15–20 shades of grey, 8 bits (1 byte) are usually sufficient to give good reproduction for standard photos. However, for digital radiographs of objects of interest in cultural heritage, (a bronze statue, for instance) 8 bits are insufficient as we have to discriminate between very close grey levels. Modern digital systems for DR can use ADC up to 14 bits and more. If we use only 2 grey levels (black and white), that is 1 bit, we will obtain a bit-map. Figure 17 shows images of the same small bust taken with decreasing bits (8, 4, 2, 1).

In the past, many mathematical techniques have been developed to improve the quality of digital images. These techniques (which will be dealt with briefly later) are related to enhancement and to the more complex field of image restoration.

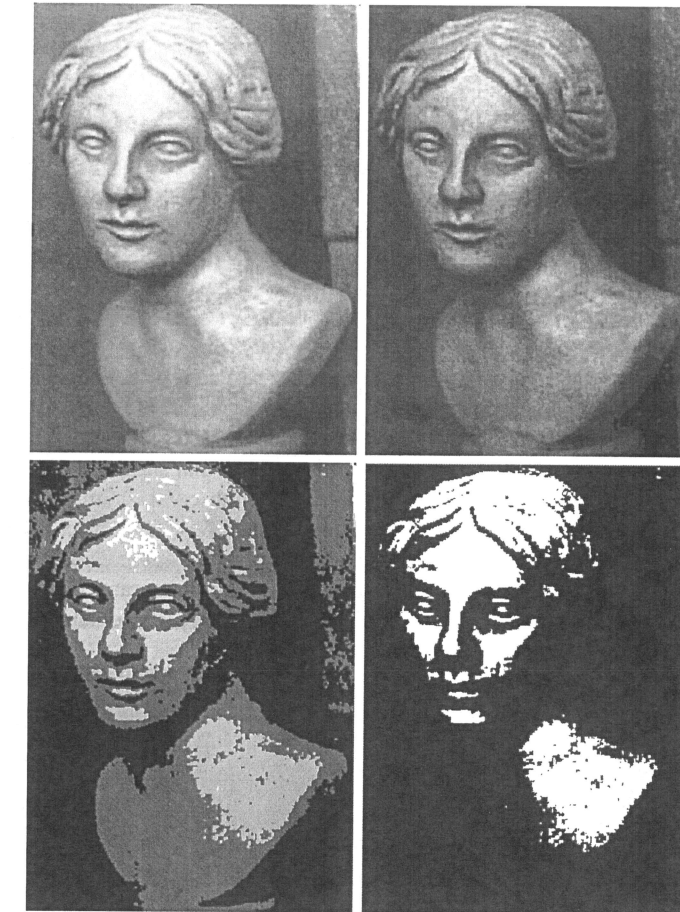


Fig. 17. The test digital image as a function of the number of bits.

4.3. Image enhancement

4.3.1. The histogram of a digital image

Let us suppose we have acquired an image “ f ” by a planar detector with M rows and N columns at 8-bit grey level. This means that our image is equivalent to a matrix of $N \times M$ numbers ranging from 0 to 255. We can now count how many pixels have a grey level, r_k , and then create the discrete function $p_f(r_k)$, named the “histogram of the digital image”, defined for 256 grey levels only.

Sometimes the histogram is given in a “normalised” form:

$$pf(rk) = nk/n \quad (8)$$

where:

$$k = 0, 1, 2, \dots, 255;$$

n_k = how many times the k -level appears in the image, that is the number of pixels having the grey level r_k ;
 n = total number of pixels ($M \times N$).

In this definition, $p_f(r_k)$ is a function with values between 0 and 1 and the integral equal to 1. Sometimes r is also normalised in the range between 0 (black) and 1 (white). Figure 18 shows the histogram of the image shown in Fig. 1.

Two different images can have the same histogram, as illustrated in Fig. 19. All histograms shown were obtained by "Adobe Photoshop" software.

For a bit map, the histogram is made by 2 segments, one that gives black pixels, the other that gives the white ones. Histograms can also be taken of colour images (one for each channel: R, G, B).

From the shape of the histogram it is possible to infer characteristics of the image. A grey image, with poor contrast, will have a histogram similar to that shown in the left image of Fig. 20 (predominance of grey levels). In contrast, a high contrast image, on the right, shows two peaks corresponding to two grey levels (0 and 255). The object is well-distinct from the background. This histogram is said to be "bimodal". Figure 21 refers to dark and bright images respectively. It is possible to operate on the histogram, pixel by pixel, by substituting a grey level, r , with another grey level, s , where s is obtained from r by a transformation law:

$$s = T(r). \quad (9)$$

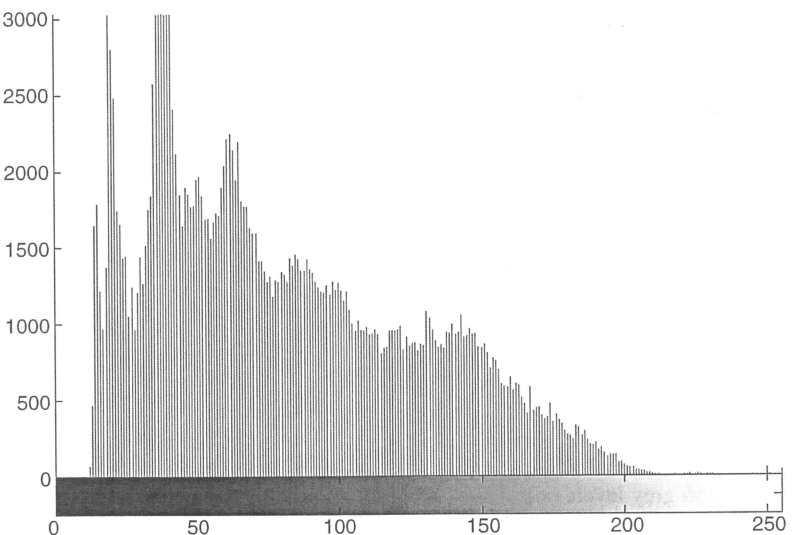


Fig. 18. Histogram of the image of Fig. 1.

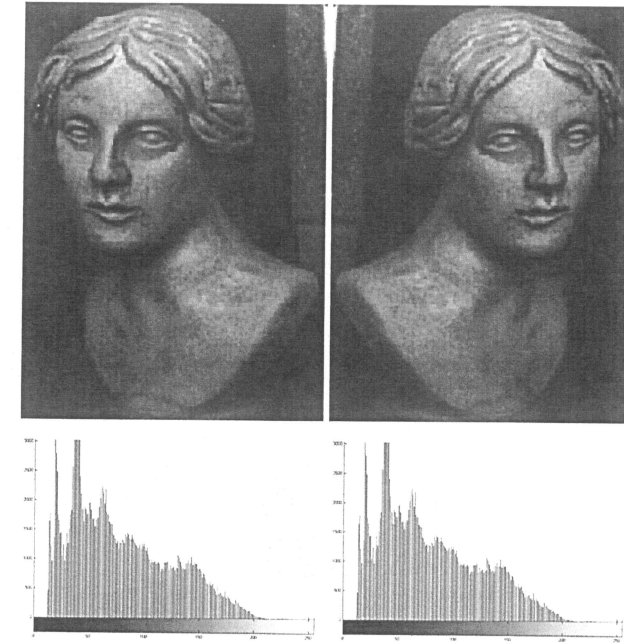


Fig. 19. Two different images (symmetric in this case) can have the same histogram.

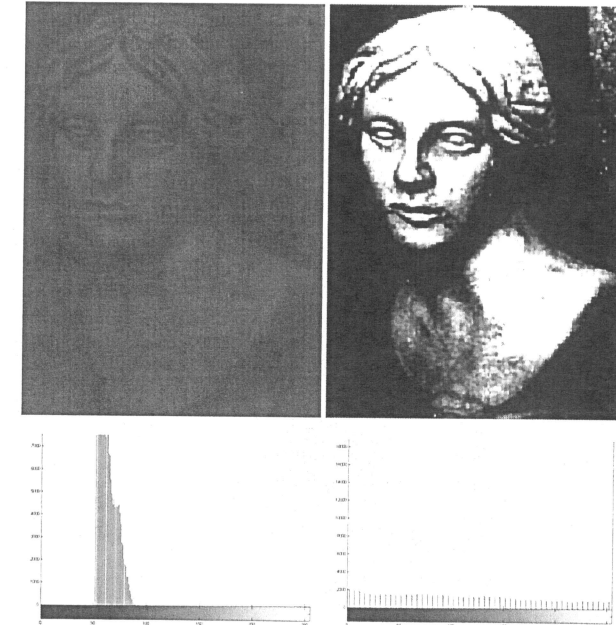


Fig. 20. Image with (left) low and (right) high contrast.

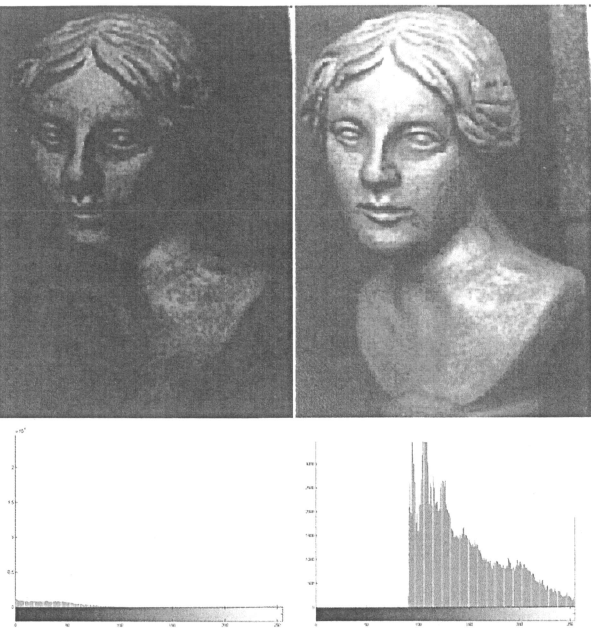


Fig. 21. Image with (left) low and (right) high brightness.

This is a “punctual operation” in the sense that it is performed on a pixel-by-pixel basis, without taking into account the “information” given by its neighbours.

4.3.2. Contrast enhancement

Working on histograms is very important for contrast enhancement. Many transformation laws ($S = T(r)$) have been proposed [13], however the simplest approach is to use the linear transformation shown in Fig. 22 where $T(r)$ is characterised by two parameters, L_1 and L_2 (the grey range is normalised from 0 to 1) only. When $L_1 = 0$ and $L_2 = 1$, the transformation is an identity (45° straight line); when $L_1 = L_2 = 0.5$, a bit-map is obtained (black and white pixels only). Other important laws are “logarithmic” and “exponential” transformation.

Another operation that enhances contrast is *histogram equalisation* (Fig. 22). Histogram equalisation aims at stretching the grey levels until they uniformly cover the entire intensity range. At the end of the operation, the histogram of the new image will be *flat*. This is true for a uniform intensity distribution. As we have discretised the intensity range, the equalised histogram will not be entirely flat and some grey levels will be lost. However, the values are far more uniformly distributed from black to white than in the original histogram and the contrast of the image is increased.

Figure 23 shows the equalised histogram, and the relative transformed image. A comparison with Fig. 1 clearly shows that the contrast has been enhanced.

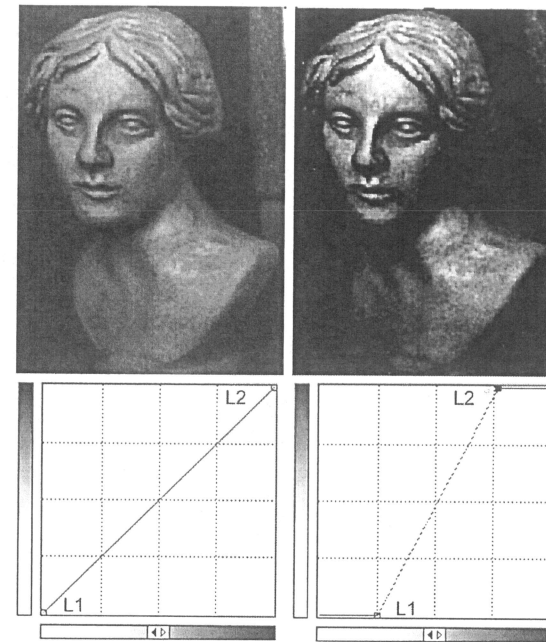


Fig. 22. Histogram equalisation, $T(r)$ as a linear function.

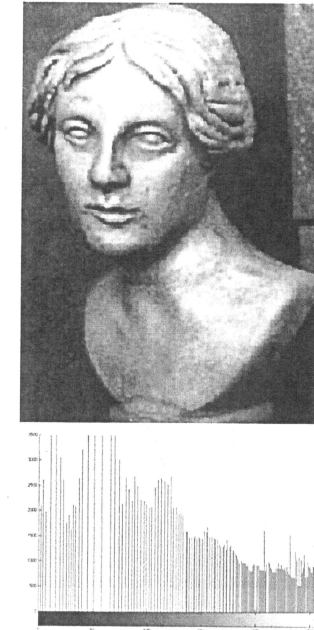


Fig. 23. Equalised histogram of Fig. 1.

$$T(r) = \begin{cases} 0 & 0 \leq r \leq L_1 \\ \frac{r - L_1}{L_2 - L_1} & L_1 \leq r \leq L_2 \\ 1 & L_2 \leq r \leq 1 \end{cases} \quad (10)$$

4.3.3. Segmentation

Segmentation is often used for a better rendering of an image with a bi-modal histogram [14]. This operation tends to detach parts of the image from the background for a better identification of them. An example is the bit-map of Fig. 17 (right-bottom). The “dark-grey” pixels, belonging to the background, have been transformed into “very-dark-grey” and the “white-grey” pixels into “very-white-grey” ones. Segmentation can also be performed for three-dimensional images. Having calculated the 3D distribution of the attenuation coefficient of the materials by computed tomography (see Section 8), one can set one material at zero density to make it completely transparent. Figure 24 shows an Etruscan bronze fibula, filled with the inner clay mould. By segmentation, applied to the histogram of the 3D image, it is possible to make the inner clay mould transparent, in order to obtain a better description of the inner bronze structure (Fig. 25) [15].

4.3.4. Frame summing

Digital images are often affected by random noise from many sources, such as the intrinsic fluctuation of photons (either from an X-ray beam or from the scintillator), the response of each pixel of the CCD, the multiplication of photoelectrons in intensified systems, and so on.

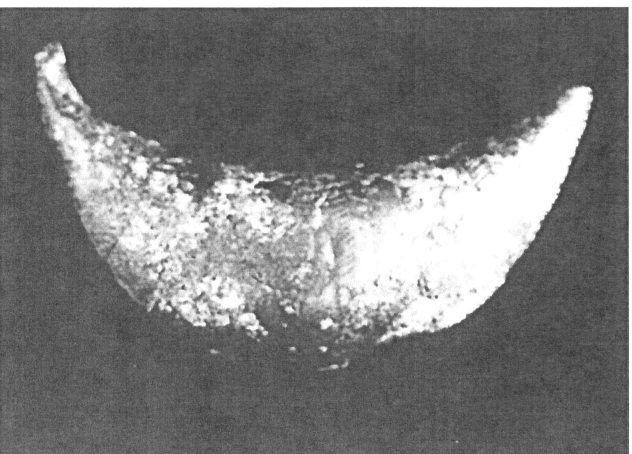


Fig. 24. Etruscan fibula (courtesy of Archaeological Museum of Bologna, Italy).

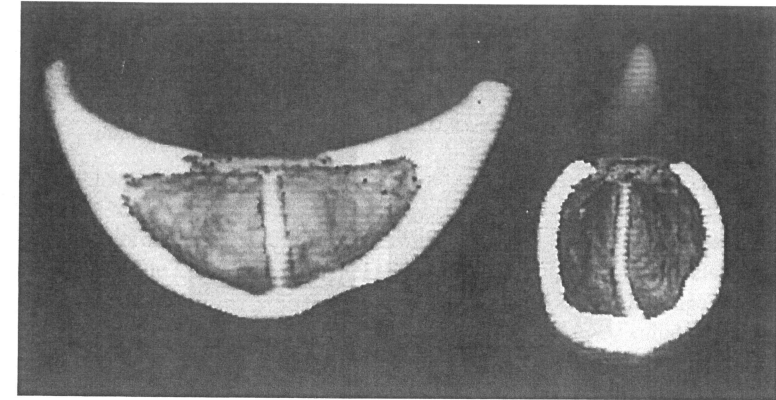


Fig. 25. CT of the Etruscan fibula (in collaboration with the Archaeological Museum of Bologna, Italy). The inner clay mould has been reduced to zero density (transparent).

This noise level determines the smallest intensity difference appreciable. Moreover, some pixels could be “blind”.

One method that can be used to increase the signal-to-noise ratio (SNR) is to sum the digitised frames. This is equivalent to increasing the integration time thus decreasing the statistical fluctuation, and is only applicable for objects that have a stationary position within the frame provided the noise is uncorrelated between frames (truly random), and the SNR increases as $(N)^{1/2}$ where N is the number of frames summed. Figure 26 shows the Fig. 1 with a “salt and pepper” noise added. Figure 27 shows the decreasing of noise after the application of frame summing (N from 1 to 6).

Warning! It is not advisable for N to be too high, as this could cause overflow and acquisition conditions could change if the time is too long.



Fig. 26. Image with induced “salt and pepper” noise.

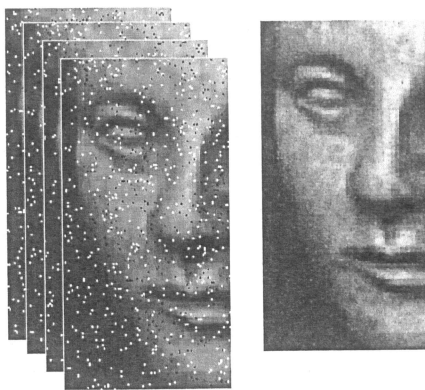


Fig. 27. Sum of different frames (up to 6).

4.3.5. Pixel binning

Detectors, most commonly linear arrays, may have a large number of pixels so that, sometimes, the image has a spatial resolution larger than desired. In such cases, it is appropriate to add the pixels of square or rectangular assemblies (usually 2×2 or 3×3) and to take the sum as a new value. Figure 28 shows images, binned in different ways. The elementary pixel increases in dimension but statistical fluctuation is considerably reduced.

4.4. Spatial filters

4.4.1. Introduction

A digital image can be “restored” just like an old painting or a noisy vinyl record. Many algorithms, known as “mathematical filters”, have been developed for performing digital



Fig. 28. The binning procedure reduces noise but increases pixel dimensions.

image restoration. Local filters and the Fourier Transform method will be discussed briefly here and readers wishing to know more about this subject should refer to specialised literature [16–18].

4.4.2. Image enhancement in the spatial domain

Two important local filters are those connected to the *smoothing* and *edge enhancement* of digital images.

Smoothing is a process whereby noise is eliminated or decreased. One procedure entails the modification of the grey level of a pixel taking into account the grey levels of the neighbouring ones (“local treatment”). For instance, a white pixel in a dark image is likely to be a mistake. The white pixel can then be substituted by the mean grey value of the surrounding pixels, properly weighted. This technique is known as “linear spatial filtering”. The larger the number of surrounding pixels, the smoother the transformed image will be. As the “smearing” of the noise decreases contrast, one can set a threshold and apply this transformation only if the difference between the original value and the transformed one exceeds this threshold. This procedure is named “medium filtering with threshold”. Another approach, which is extremely useful in the case of “salt and pepper” type noise, is the so-called “median filter”, consisting in taking the pixels of the neighbourhood being processed, ordering their grey values from smallest to largest, then taking the median value and using it to replace the original one (Fig. 29). Unlike the “medium filter”, this filter maintains the boundaries but is not of a linear type.

Enhancement is a process whereby the difference between the zones of the image is enhanced. As smoothing is a sort of averaging (integral over a zone), enhancement will be obtained by applying the inverse operation, which is the derivative (gradient or laplacian operators). A threshold may also be imposed for these filters. For an optimal result, it is advisable to operate using several filters in sequence [19,20].



Fig. 29. Figure 26 “cleaned” using a median filter.

4.4.3. Fourier-Transform-based filtering

For a better comprehension of this mathematical approach, let us start from the treatment of an acoustic signal, for instance a sound produced by an orchestra. Sound can be intended as a combination of many harmonics with different frequencies: the cello is characterised by low frequency harmonics, violins are characterised by higher frequency ones.

The whole of harmonics is called as the spectrum, which completely characterises the sound. If we use a proper electronic filter to decrease the high frequencies, we conversely increase the importance of the lower ones, that is the cellos. By decreasing the lower ones, we enhance the violins, and so on. The noise of an old vinyl record is also characterised by high frequency harmonics. So, if we develop in harmonics the sound of the record, then apply a filter to reduce the higher frequencies, we "clean" the sound of the noise. This mathematical procedure derives from the well-known development in Fourier series (see Appendix A).

One can proceed in much the same way with digital images. However, instead of using the development in Fourier series, and as a digital image is a discrete function, a more suitable mathematical approach, the FFT algorithm (Fast Fourier Transform), is used [21]. We can now modify the spectrum. If we decrease the high frequencies and let the low ones pass, we decrease the noise (equivalent to smoothing); conversely, if we decrease the low frequencies, we increase the importance of the rapid spatial variation, *i.e.* we enhance the boundaries. For images with unique characteristics, it is possible "to design" specific digital filters.

Unlike local filters, Fourier filtering treats images as a whole. These matters are dealt with in greater detail in Appendix A and, to an even greater extent, in the many books dedicated to them [18,22].

Mathematical software is commercially available to perform all these filtering operations.

5. DETECTORS FOR X- AND γ RAYS

5.1. Families of detectors

It is possible to classify detectors into seven families.

1. *Gas-filled detectors* (for instance, argon at high pressure). These appliances were used in systems for medical applications. They have a very low efficiency but a very high dynamic range. Nowadays, they are used primarily in a number of industrial applications.
2. *CCD (Charge Coupled Device)-based detectors* are constructed of a semiconductor, usually silicon, in which the light produces pairs of electrons and vacancies. The CCD is like a pixel matrix; the higher the photon number, the higher is the charge collected in the single pixel. By measuring the charge collected in each pixel, and representing the measured value in binary form, one obtains a digital image. CCDs are also sensitive to X-ray photons that arrive directly on the silicon matrix. In such cases, the image is affected by undesired white zingers.
3. *Scintillation detectors*, consisting of a fluorescent material which emits light when exposed to X-radiation (*e.g.* CsI and $\text{Gd}_2\text{O}_2\text{S}$), are very widely used. The fluorescent material:
 - (a) can be smeared directly (or indirectly through optical fibres) over a light detector (for instance, photodiode arrays or photomultiplier);
 - (b) can be smeared over a screen optically coupled to a CCD camera by a lens. A mirror, usually angled at 45° , makes it possible to keep the CCD camera out of the beam.

4. *Semiconductor detectors* (*e.g.* CdTe, CdZnTe, HgI, and Ge) allow direct photon counting with its energy, if required. Using this type of detector, it is possible to perform "gamma spectrometry". This type of equipment can be used for high energy X-ray imaging, which has a high dynamic range but a low spatial resolution (pixels no smaller than 0.5 mm).
5. *Image intensifiers* (I.I.) are based on rare earth screens from which the X-ray photons extract electrons, which, in turn, are accelerated by an electric field onto a fluorescent screen. A very bright image forms on the screen and is acquired by a CCD camera through a lens. Using I.I., it is possible to obtain digital images with low dose levels and therefore, they are often used in medical diagnostics. They have a low dynamic range and certain image distortions. One type of I.I. is the EBCCD (*Electron Bombarded CCD*) in which the extracted electrons are directly accelerated against a CCD without the lens coupling [23]. EBCCDs have smaller dimensions than standard I.I.s. Moreover, EBCCD can be fitted with a lens extending the range of the field of view (from small to large light source as a scintillating screen $30 \times 40 \text{ cm}^2$).
6. *Flat panel* is a radiation detector of planar geometry which consists of a matrix of very small detectors (pixel with sides of 100 micron or less). They are made by amorphous selenium (Se-am) or with amorphous silicon (a-Si). In the Se-am version, the X-ray photons interact directly with the Se producing free charges, which are read by suitable electronics. In the a-Si version, a layer of scintillator (*e.g.* GOS or CsI) produces light which is read by a matrix of underlying sensors when bombarded by X-rays [24].
7. *CMOS (Complementary Metal Oxide Semiconductor)* is very similar to a flat panel. It is mainly composed of a matrix of microprocessors covered by a layer of scintillator (typically GOS or CsI). The light produced by X-ray interaction is transformed into electrical signals read by the underlying microprocessors. This type of detector needs a small amount of energy, which makes it suitable for transportable equipment, and are very fast. The pixel side is of the order of 90 microns and they can be assembled in "buttable" mode. This type of equipment could become the detectors of the future, at least for low energy photons.

Appendix C shows the characteristics of some flat panels, now (end 2004) on the market, and the features of a system based on a CCD camera coupled with a scintillating screen.

5.2. Geometry of the detection systems

Digital image acquisition systems can be listed in several ways. Below, reference will be made to their geometrical shapes: single detector, linear array of detectors, (planar) two-dimension detector.

5.2.1. Single detector (*point geometry*)

Usually in this case, the detector receives the radiation through a narrow collimator (Fig. 30). This detection assembly is very useful in decreasing diffused radiation. Very good systems

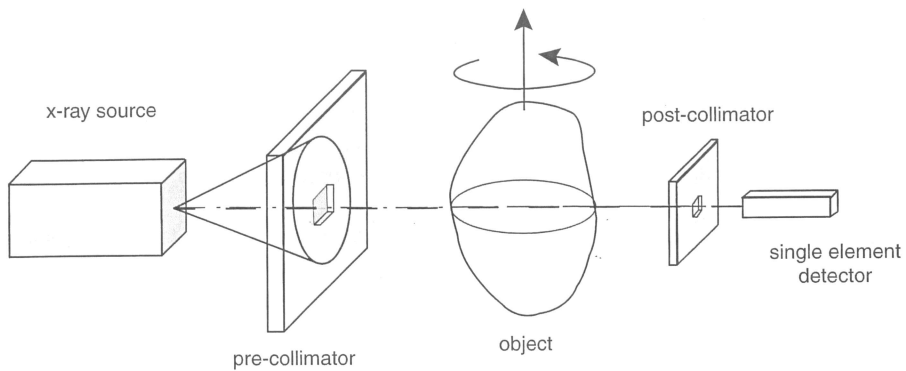


Fig. 30. “Pencil-beam” acquisition system with a single element detector.

are available on the market, mainly for medium and high-energy X-ray CT, with many single detectors each of which is well-collimated. The images are very sharp but acquisition times are rather long.

5.2.2. Linear geometry (linear array)

This assembly is also known as a “linear array detector”; it is composed of several single detectors (of the order of one thousand or more) positioned close to one another (Fig. 31) so that a “line” of object under investigation is obtained with a radiation shot. By moving the object linearly in front of the detector and “adding” the single lines, we obtain a matrix of pixels, that is a digital image as described in Section 4.2. The equipment used to check hand luggage in airports, has one or two linear array detectors (for looking from different angles). The source is usually collimated through a slit (fan beam). The collimation of the whole system is not as good as in the previous case but there is the advantage of a faster acquisition speed.

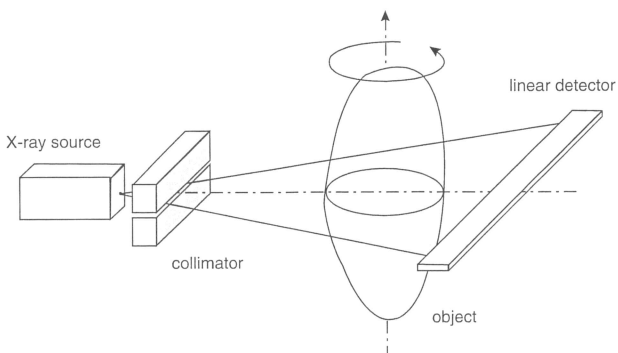


Fig. 31. “Fan beam” acquisition system with a collimated beam and a linear array of detectors.

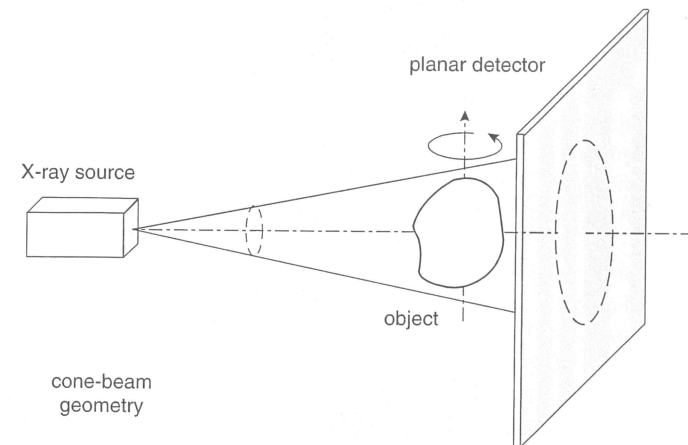


Fig. 32. “Cone beam” acquisition system with a broad beam and a planar detector.

By rotating the object in steps and making a radiation shot for each angular step, it is possible, after proper mathematical treatment, to reconstruct a “slice” of the body. A contemporary translation and rotation of the object gives so-called “spiral CT”. Modern medical CT equipment is always of the “spiral” type [25].

Often, instead of having a single array of detectors, many detectors are packed together. In this case, we have multi-slice CT.

5.2.3. Bidimensional geometry (planar detector)

The image (shadow) is produced by a broad beam, named *cone beam*, over a planar detector, which can be a flat panel, a CMOS or a scintillating screen viewed by a CCD camera (Fig. 32). With this kind of system, a digital radiography (DR) is obtained with a single shot. By rotating the object and acquiring several DRs, after proper mathematical treatment (see Section 8.2), three-dimensional tomography of the object is obtained (*3D cone beam CT*).

5.3. The Modulation Transfer Function (MTF)

If we have a hi-fi radio, we can correctly reproduce either low or high frequencies (e.g. drums). However, if we have bad equipment, we will not be able to obtain quality sound reproduction, especially for high frequencies, as our radio “cuts out” part of the high frequencies. The same happens with a camera lens if the details of an image are too close. In order to quantify the quality of the lens, we can give the number of pairs of lines (succession of black and white) that our lens is able to separate. For this reason the spatial resolution of a lens is given in lp/mm (line-pairs per mm), which is a “spatial” frequency. The same approach is adopted for digital acquisition systems. Figure 33 shows a sequence of lead bars named

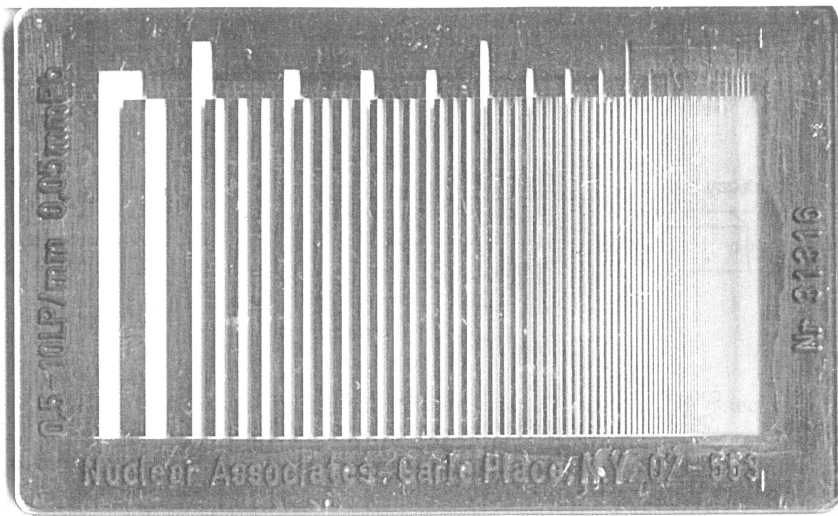


Fig. 33. Photograph of a line-pair gauge.

“line-pair gauge” with decreasing distances between one another. If we take an X-ray radiograph of this line-pair gauge (see Fig. 35) we will see that over a certain spatial frequency, our system is not able to separate the lead from the void. The Modulation Transfer Function (MTF) indicates the percentage of a modulated signal that our system will allow to pass. The higher the frequency, the lower the percentage will be. It is therefore possible, for each system, to create this function, which generally speaking, will decrease monotonically with spatial frequency, as in Fig. 34.

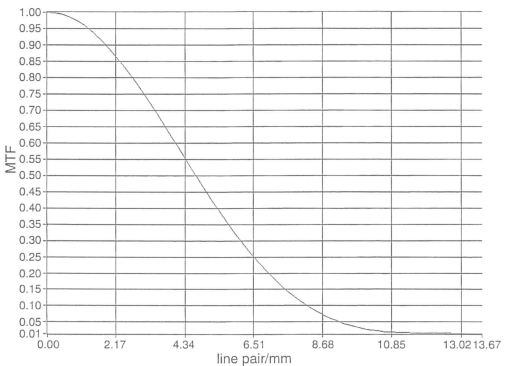


Fig. 34. Example of MTF.

By observing this figure, we notice that at the frequency 13.7 lp/mm, the MTF becomes zero (the “cut” frequency); moreover MTF is 0.5 (50% of signal passes) at 4.6 lp/mm and it is 0.05 (5%) at about 9 lp/mm. Therefore, when speaking of the MTF of a system, one must specify what the assumed percentage is. For instance, if a system has an MTF (5%) of 2 lp/mm, it means that it is possible to distinguish a detail of the dimension of 250 μm with a difference in grey of 5% from the background. If we have a complex system, like a chain for DR acquisition (X-ray source, scintillating screen, CCD camera, computer monitor and so on), the MTF of the system will be the product of the MTFs of each component.

Warning! It is useless to have one very good system component when another has poor qualities. If we consider a system with 2 components; the first of which has an MTF of 0.2 and the second an MTF of 0.8, then the system’s MTF is 0.16. If we now consider a second system similar to the first, with components of MTF 0.5 and 0.5 respectively, the total MTF of this system is 0.25, that is better than the previous one.

Figure 35 shows the DR of the line-pair gauge, taken by a CMOS detector with a microfocus at 110 kV and 1 mA [26]. From this figure, it is possible to evaluate the MTF of the system.

Methods for calculating and measuring the MTF of a system are given in Appendix B.

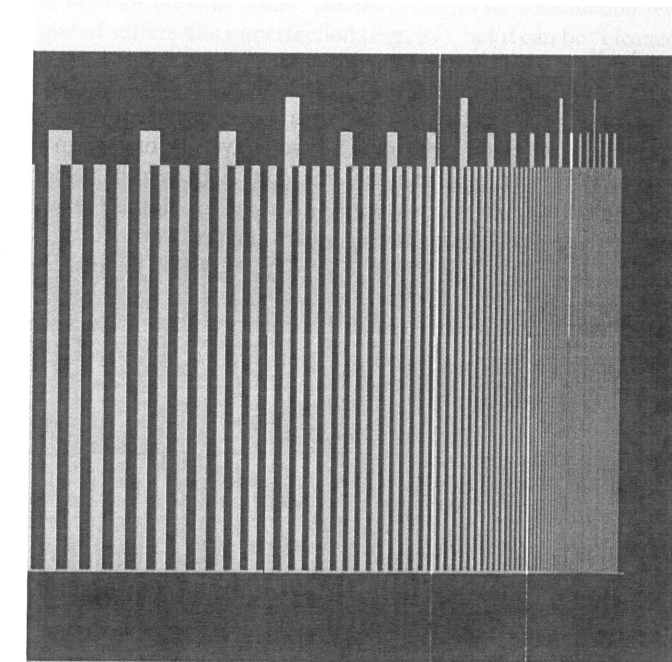


Fig. 35. X-ray radiography of line-pair gauge of Fig. 33.

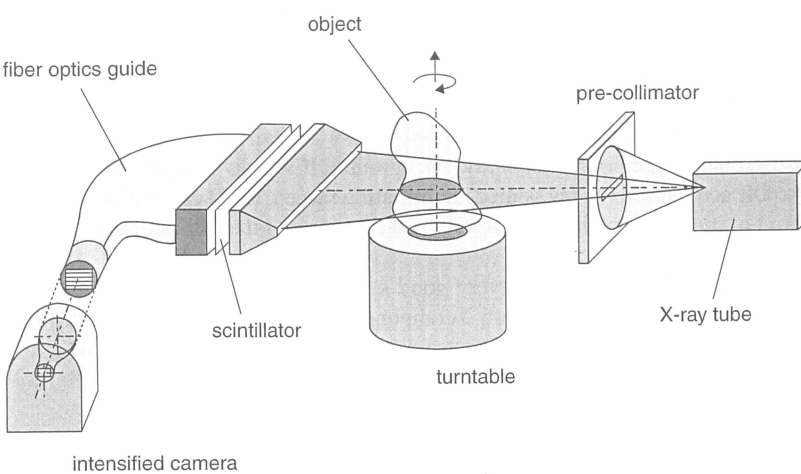


Fig. 36. Diagram of the linear array system.

6. EXPERIMENTAL ACQUISITION OF DIGITAL RADIOPHOTOGRAPHS: SOME EXAMPLES

6.1. Acquisition by linear arrays

Detectors of linear array type are often used to obtain high resolution Digital Radiographs. A sketch of a new linear detector, developed by the University of Bologna, is shown in Fig. 36. It consists of a fibre optic (FO) fan that transports light over the photocathode of an EBCCD. The fan is made of seven ribbons as positioned in Fig. 37; this FO fan is a “geometry transducer”, in the sense that it changes the geometry of the active area of the EBCCD from 1024×512 to 5607×60 pixels, thus obtaining a large (5600 pixels), multi-slice (60) detector.

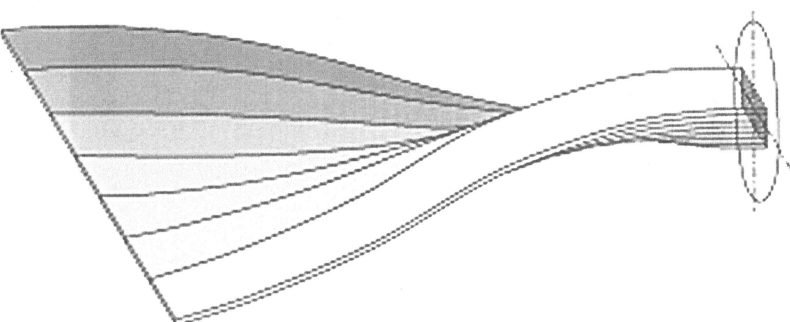


Fig. 37. Picture of the linear detector. An FO fan is coupled with the photocathode of an EBCCD.



Fig. 38. The rear of an FO fan with patterns due to construction.

The image collected appears as a sequence of many slices that are rearranged to give one wide slice. The detector presents some “patterns” due to its construction feature (Fig. 38). The image acquired suffers this imperfection (Fig. 39), but it can be “cleaned” by subtracting the patterns (Fig. 40).

The DR is obtained as a sequence of many slices, as in the case of scanners. As the light converges over an EBCCD, the detector acts as an image intensifier so that the system can

the grain connections
 er are the specific area.
 g the state of a snow lay
 nt parameters describing
 properties. The importai
 ds will govern the snow
 le quality of the ice bon

Fig. 39. The image affected by the pattern background.

the grain connections .
er are the specific area.
g the state of a snow lay
nt parameters describing
properties. The importan
ts will govern the snow
ne quality of the ice bond

Fig. 40. The image of Fig. 39 “cleaned” of the pattern background.

perform DR with a far lower radiation dose than in standard films. If lower doses are essential for human beings, they are also advisable for paintings.

The aforementioned linear array was used as shown in Fig. 41 for the DR of a painting, a “test painting” with different pigments and cements prepared by the Opificio delle Pietre Dure in Florence. The high spatial definition of the detector allows the identification of the linen weft (see Fig. 42). Moreover, by making use of enhancement filters, it is possible to investigate either the painting or the frame with one shot alone, which is not possible with films that need different X-ray tube voltages. Another important feature of this detector is that the geometrical distortion, connected with film, is minimised with this geometry. By moving the detector and the X-ray tube synchronously with suitable equipment, it would be possible to easily “scan” a large painting and store all the high definition data on electronic media (*e.g.* DVD).

6.2. Acquisition using planar detectors

Of the many planar detectors suitable for acquiring digital images, the system that the Department of Physics of the University of Bologna and the Getty Conservation Institute have jointly developed is described below. It was designed for digital radiography (DR) and computed tomography (CT) to analyse objects of artistic interest. The system, designed to be used with a 450 kV X-ray tube, consists of an L-shaped aluminium box with a scintillator screen ($44 \times 44 \text{ cm}^2$) of CsI(Tl), 1 mm thick, a mirror and a cooled CCD camera (Fig. 43). The image formed by the X-ray beam on the screen is viewed by the CCD camera (2184×1472 pixels) *via* the mirror angled at 45° . The CCD camera is

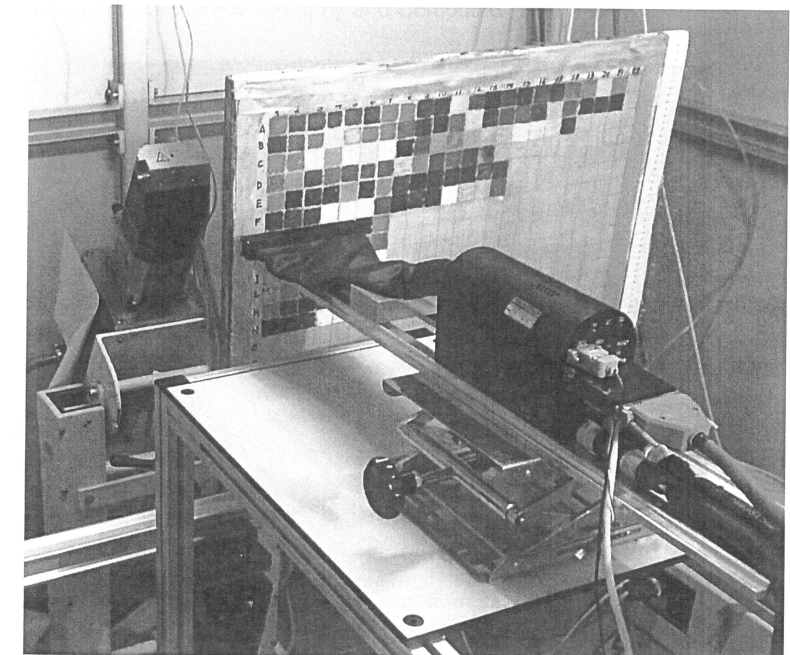


Fig. 41. The linear detector ready to perform a DR of a painting.

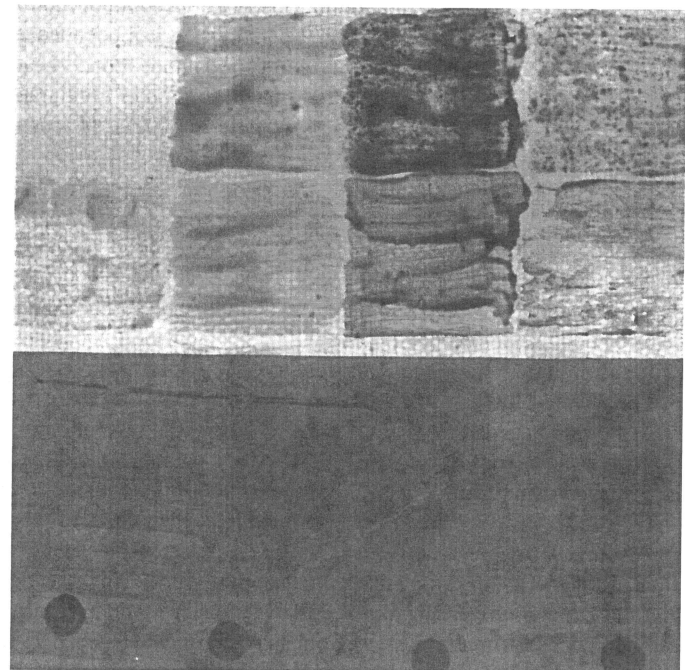


Fig. 42. Detail of the DR taken of the linen weft of the painting in Fig. 41.

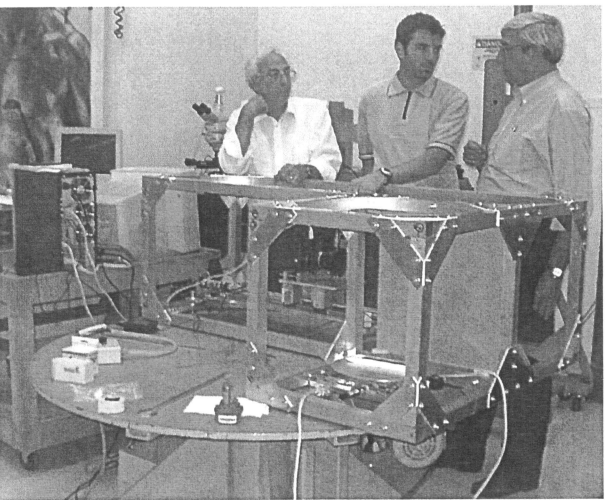


Fig. 43. The DR and CT system at the Getty Conservation Institute (GCI).

equipped with high aperture lenses. This feature of the system enables the detection of details smaller than 300 µm. Great effort was made to reduce the importance of the radiation diffused by the objects under investigation. This kind of radiation increases blurring and, conversely, decreases the contrast of images. The system has been tested on objects of different shapes and composition. Figure 44 shows a Roman bronze head in front of the scintillator and the Fig. 45 shows the acquired image. Computer tomographs, acquired by this system, are shown in Section 9.3.2. More details of this system are given in Appendix C.

6.3. The advantages and disadvantages of digitising

As mentioned above, a digital image is equivalent to a matrix of numbers and, therefore it can be saved (in CD or DVD) for a long time without degrading (in theory!), unlike the radiographic film. A digital image can be transmitted via the Internet and can be processed to reduce noise or increase the contrast as explained in Section 4 and in Appendix A. On the other hand, a digital image usually cannot achieve the spatial resolution of an analogue image. However, with modern CCD cameras, it is possible to get submicrometric resolution that cannot be achieved using film.

Warning! Since the 1950s, great changes have taken place in electronic storage with the introduction of magnetic tapes, optical disks, floppies, CDs, DVDs, which has led to great suffering and expenditure when one needs to recover something old (from image storing point of view) or when translating data from an old format to a new one. It is therefore preferable, when possible, to save data also in an analogue format that can be treated easily

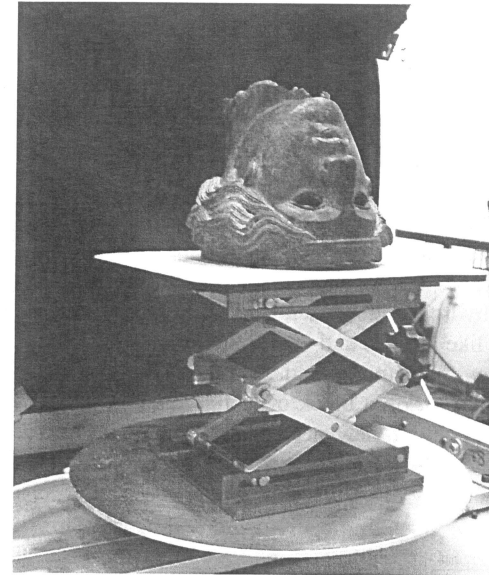


Fig. 44. Photo of the head of an ancient Roman statue in front of the planar detector at the GCI.



Fig. 45. X-ray of the head in Fig. 44.

in future or updated from old to new format should this still be feasible. In the future, this conversion could be dramatic!

7. DIGITAL IMAGING FOR NEUTRON RADIATION

7.1. General considerations

Unlike photons, which interact primarily with the electrons of atom shells, neutrons interact with atomic nuclei and as a result, a different kind of reaction is to be expected. When interacting with matter, neutrons are removed from a beam (by absorption or scattering) by light elements, like hydrogen, deuterium and carbon, or by particular isotopes with high capture cross sections, like ^{10}B , ^{6}Li and ^{155}Gd . Figure 46 shows the linear absorption coefficient of some isotopes for neutrons and X-rays [27]. Using neutron radiography, it is possible to see a plastic film on a block of lead, which would be absolutely impossible using X-rays. From this point of view, neutron radiography may be considered as “complementary” to conventional radiography. As neutrons have no charge, their detection is based on the indirect ionisation they produce.

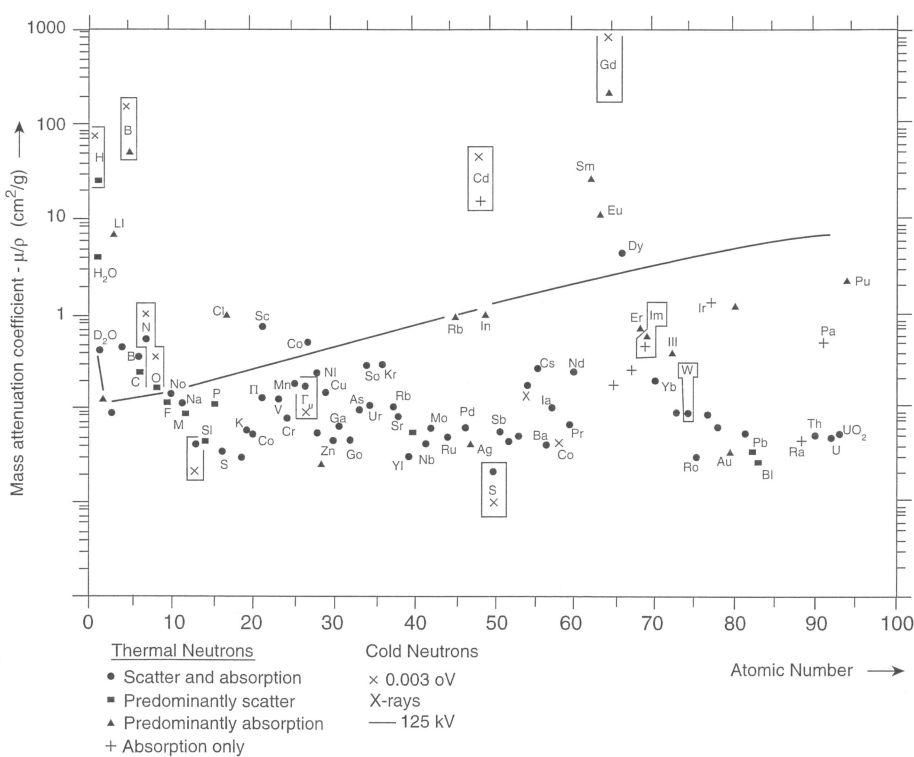


Fig. 46. Neutron and X-ray mass attenuation coefficients for neutrons and X-rays [27].

The most important reactions used, for imaging purposes, are:

- (a) $n + {}^6\text{Li} \rightarrow {}^3\text{H} + \alpha$, with kinetic energy of reaction products of about 4.79 MeV;
 - (b) $n + {}^{10}\text{B} \rightarrow {}^7\text{Li} + \alpha + \gamma$ with kinetic energy of reaction products of about 2.79 MeV;
 - (c) interaction [neutron \rightarrow proton] with detection of proton;
 - (d) $n + {}^3\text{He} \rightarrow {}^3\text{H} + p$, with kinetic energy of reaction products of about 0.764 MeV;
 - (e) interaction [neutron + fissile nucleus], with kinetic energy of fission products of about 200 MeV.

Reactions (a) and (b) are used for the detection of so-called "thermal" (with $E_n < 0.4$ eV) and "epithermal" neutrons (0.4 eV $< E_n < 100$ keV); reaction (c) is for fast neutrons ($E_n > 0.5$ MeV), and reactions (d) and (e) are for both thermal and fast neutrons.

7.2. Planar detectors for neutrons

For digital neutron imaging, the most common detectors are planar models (see Section 5.2.3). In particular, for thermal neutrons, scintillating screens smeared with a mixture of ^6Li and ZnS are used [28]. The neutron is absorbed by ^6Li , thus producing an α particle and a triton which dissipate their kinetic energy in the ZnS, creating a light flash (see reaction (a)). The light can be recorded by a CCD camera [29]. For neutron radiography, ^{10}B loaded film can also be used [30].

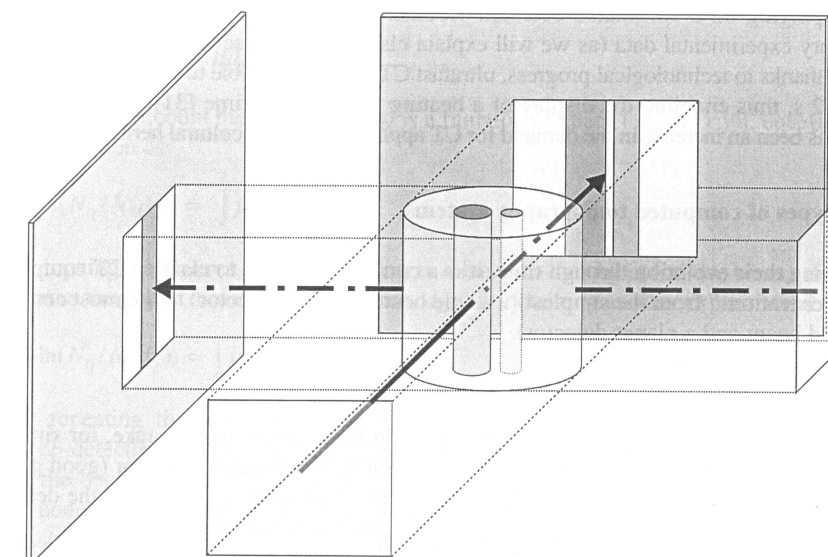


Fig. 47. Two projections, taken at right angles, show how some details are not visible in one of them. In order to overcome this drawback, computed tomography is based on a set of very many projections and enables the correct reconstruction of the complete section or volume.

As mentioned previously, the advantage of neutron imaging is that it is able to detect organic material traces in metallic objects such as corrosion or inner clay mould or internal wooden parts.

8. COMPUTED TOMOGRAPHY USING X-RAYS AND GAMMA PHOTONS

8.1. General considerations

Let us consider a cylindrical vessel containing two smaller cylinders. Two radiographs (projections) of this object are shown in Fig. 47; it goes without saying that what we are able to see of the content of the vessel depends on the projection angle. For instance, in the projection on the left, the smaller cylinder is covered by the larger one. If, instead of having projections on one plane, we virtually cut the container and consider its “section”, known as a “slice”, we can see both inner cylinders. This operation of “cutting” is named “tomography”, from the Greek meaning “to cut”.

The problem of how to obtain a section of an object using an infinite set of rays passing through it, was solved theoretically in 1917 by the Austrian mathematician Radon. However it was not until the 1960s that two scientists, the physiologist Geoffrey Hounsfield and the physicist Allan Cormack (separately) succeeded in obtaining the section of an object experimentally.⁵

The first equipment consisted of a gamma beam (a radioisotopic source, inside a collimator) impinging on a collimated detector. Hounsfield took several days to collect all the necessary experimental data (as we will explain elsewhere), and several more to process it. Today, thanks to technological progress, ultrafast CT systems are able to acquire slices in less than 0.2 s, thus enabling the display of a beating heart in real time [31]. In recent years, there has been an increase in the demand for CT applications in the cultural heritage sector too.

8.2. Types of computed tomography systems

Following their evolution through time, it is a common practice to classify CT equipment into “generations” from the simplest (a single beam and one detector) to the most complex (a broad beam and a planar detector).

8.2.1. First generation CT system

Following the procedure adopted by Hounsfield in his experiments, we take, for simplicity, a collimated monoenergetic gamma source seen by a collimated detector (good geometry conditions) as in Fig. 48. Let N_0 be the number of photons impinging on the detector having run the chord d_1 of the object. From equation (6), we obtain:

$$N(d_1) = N_0 \exp(-\mu d_1).$$

⁵ For the development of Computed Aided Tomography, G.N. Hounsfield and Allan M. Cormack received the Nobel Price for Medicine in 1979.

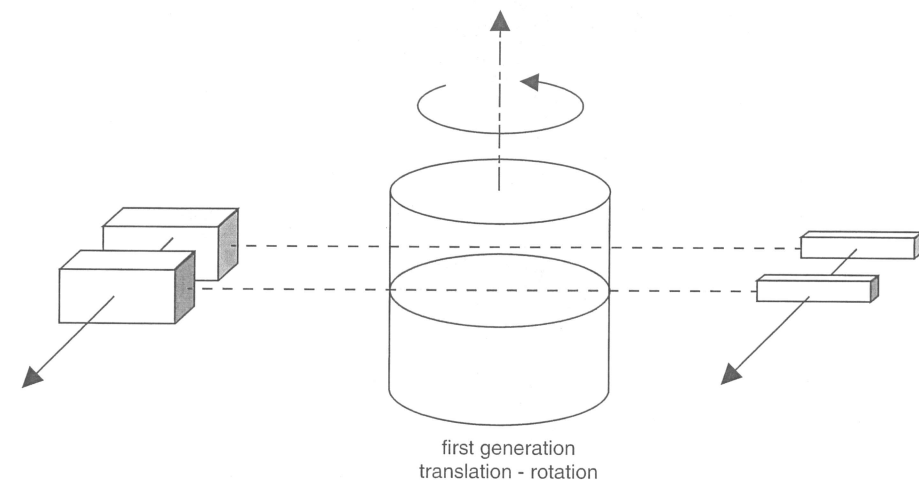


Fig. 48. First generation tomography system: a single detector scanning the object at each angle (translation and rotation).

From which one gets:

$$\ln(N_0/N(d_1)) = \mu d_1. \quad (11)$$

Taking into account that, in general, μ is a function of space ($\mu = \mu(x, y)$), equation (11) may be written as:

$$\ln(N_0/N(d_1)) = \int \mu(x, y_1) dx. \quad (12)$$

By moving the “source-detector” system in relation to the object (or *vice versa*), the beam will cross the object through another chord, d_2 , thus obtaining another experimental value:

$$\ln(N_0/N(d_2)) = \int \mu(x, y_2) dx. \quad (13)$$

By repeating the same operation for many chords and rotating the object (or the “source-detector” system) by a small angular step ($\Delta\phi$), then repeating the measurements from the beginning several times, one obtains a “net of beam-rays” covering the whole slice under investigation. Using a proper mathematical procedure [32], it is possible to reconstruct the function $\mu(x, y)$, that is the absorption linear coefficient of the body under examination.

As the number of measurements cannot be infinite, the function $\mu(x, y)$ is not continuous but rather “pixelised”, like a digital image. The smaller the linear step (Δd) and angular step ($\Delta\phi$), the better the $\mu(x, y)$ reproduction will be. As the beams are parallel, it is sufficient to rotate the object through 180° . This procedure is known as “first generation CT”.

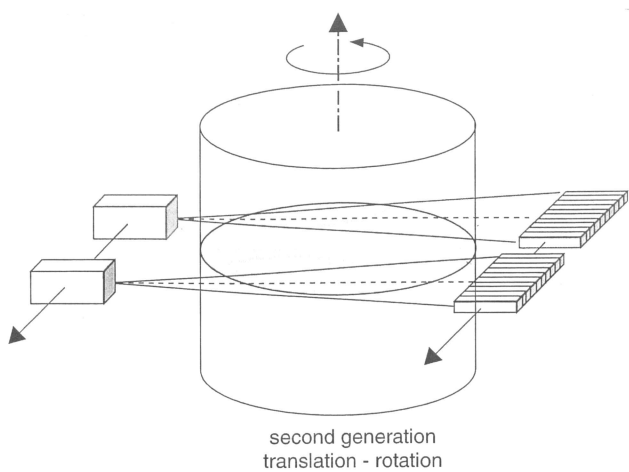


Fig. 49. Second generation tomography system: a linear array of detectors scanning the object at each angle through 360° , but with a lower shift number (translation and rotation).

“Thumb rule” The number of angular steps should not be less than the number of linear steps.⁶

8.2.2. Second generation CT system

Although first generation systems are the most correct with regard to image reconstruction, they require lengthy timeframes. In order to reduce acquisition times, instead of a single detector, an array of N detectors is used (Fig. 49) (see Ref. [33]), which is equivalent to performing N measurements at the same time. With this type of detector, the translation step number decreases (but the number of rotation steps does not). This type of system is known as “second generation CT” equipment.

As, unlike first generation systems, the beams are not parallel, rotation must be performed through 360° . When a “synchrotron light” is used as a radiation source, the rays are parallel and consequentially, rotation is through 180° .

The equipment used for the CT of large objects (for instance, rockets), are often second generation models [34,35].

8.2.3. Third generation CT system

If the linear array is wide enough for the whole object to be projected over it (see Fig. 50), rotation alone is needed. If rotation and translation – in direction perpendicular to the rotation plane – are performed simultaneously, we can produce “spiral CT”. This type of CT is suitable for cylindrical objects such as a column, rock core or human body.

⁶ It can be demonstrated that, for having good results for the reproduction of the outer part of the object under examination, the optimal number of the angular steps should be about $\pi/2$ times the number of the linear steps.

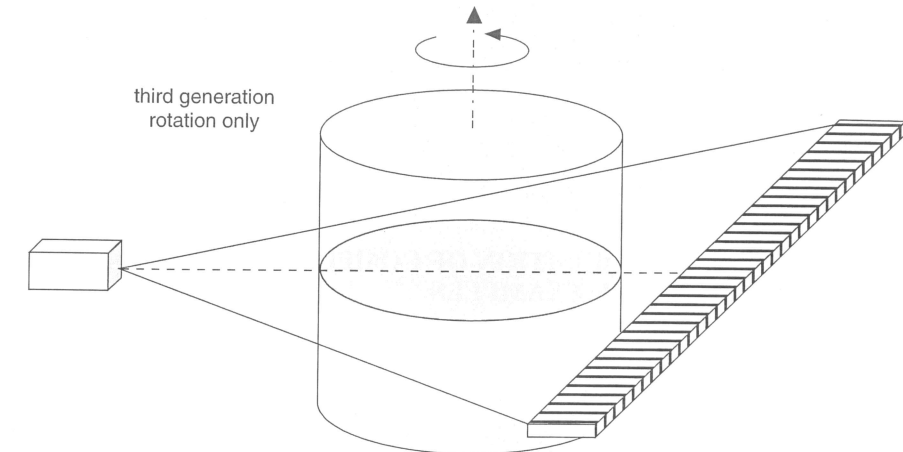


Fig. 50. Third generation tomography system: a wide linear array of detectors collects the projection of the complete section of the object at each angle through 360° . It is no longer necessary to move the detector (rotation only).

8.2.4. Medical CT

Almost all new CT systems for medical diagnostics are of the spiral type. In this type of systems, the detectors are located on a circumference that surrounds the cavity in which the human body moves. The X-ray tube rotates continuously irradiating part of the detector ring. In modern CT, there are several rings of detectors, named “multi-slice system” (e.g. see Ref. [36]).

Warning! Medical CT is suitable for use in the cultural heritage field when the object examined has similar characteristics to those of a human body, such as Egyptian mummies, wooden statues, etc. it goes without saying that it is not possible to acquire tomographs of metal objects (such as bronze heads) due to the low penetration of the X-rays of these tubes (maximum voltage of the order of 160 kV).

8.2.5. “Cone beam” tomography

To increase the acquisition speed, the source beam – in the shape of a cone – totally irradiates the object that rotates in front of a planar detector (Fig. 32). If the detector is smaller than the projection, a macro-slice of the object only is acquired. In order to obtain a CT of the entire object, it is necessary to move the object vertically and acquire several macro-slices that are later “joined” together using a dedicated software programme. This approach is called the “cone beam tomography” and it is often used to inspect pieces of archaeological interest. The disadvantage of cone beam tomography is the high percentage of diffused radiation that impinges on the detector, as no post-collimator is present. Like planar detectors, they

can use flat panels, a scintillating screen seen by a CCD camera or CMOS covered by a suitable scintillator. The FDK algorithm is usually adopted for image reconstruction [37]. (FDK is an acronym of the initials of Feldkamp, Davis and Kress, the authors of [37].)

Warning! For this approximation to be valid, the aperture of the cone angle must be not greater than 10°.

9. EXPERIMENTAL ACQUISITION OF COMPUTED TOMOGRAPHS: SOME EXAMPLES

9.1. Foreword

Until a few years ago, computed tomography was a diagnostic technique applied mainly to human beings. With the development of different types of detectors and the lowering of costs, this technique is now also more widely used in the cultural heritage field. However unlike the human body, the dimensions of objects of cultural interest cover a wide range: from a prehistoric tooth, just a few millimetres long, to large globes with diameters of over 2000 mm. It is therefore necessary to develop different kinds of CT systems, each one specialised in a particular type of object. Descriptions are given below on the different kinds of equipment developed, considering cultural heritage requirements only.

9.2. Microtomography

9.2.1. Microtomography in cone beam geometry

If the object under investigation is small (few mm) and if a good spatial resolution is required (of the order of few microns), then a micro-tomographic system is used (μ -XCT). In this type of system, phosphor is smeared over FO tapers, or FO ribbons or directly over the CCD. A microfocus or nanofocus is used as an X-ray source (see Section 2.3.1). When available, synchrotron light constitutes a very efficient source (see Section 2.3.3). A μ -XCT system is shown in Fig. 51 [38]. It has a field of view of $30 \times 15 \text{ mm}^2$. Figures 52 and 53 show the CT of an ancient Roman tooth and a fossilised jaw acquired using this type of CT system [39]. A fine focus tube was used as the X-ray source and it has a focal spot ranging from 5 to 100 μm (depending on the power), maximum voltage 200 kV and maximum current 2 mA.

9.2.2. Microtomography with a linear detector

The detector described in Section 6.1 was also used in CT configuration (see Fig. 38). Using a synchrotron ELECTRA (SYRMEP beam-line) as an X-ray source, it was possible to obtain a multi-slice CT of a human femur with a spatial resolution comparable to that of a small bone fragment (see Fig. 54) and this slice constitutes one of the largest objects tomographed with this kind of spatial resolution [40].

If one requires very high spatial resolution, it is possible to use a single crystal of scintillator viewed by a microscope equipped with a CCD camera.

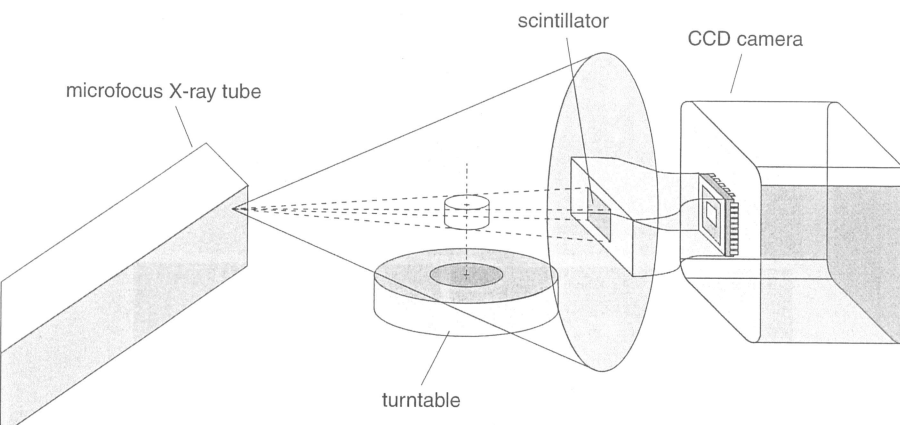


Fig. 51. Diagram of an experimental microtomography system. A cooled CCD camera is optically coupled with a scintillating material layer by means of a fibre optic taper in a cone-beam geometry.

9.3. Medium-size CT systems

Medium-size CT systems have screens ranging from $30 \times 30 \text{ cm}^2$ to $40 \times 40 \text{ cm}^2$, using either a flat panel (see Section 5.1) or a home-made system, the features of which can be adapted to suit user needs. Two home-made systems will be described here.

9.3.1. CT system with EBCCD

This system has a GOS scintillating screen $30 \times 30 \text{ cm}^2$; the image produced on the screen by the X-ray beam is viewed by a 1024×512 pixel EBCCD camera. As this camera is

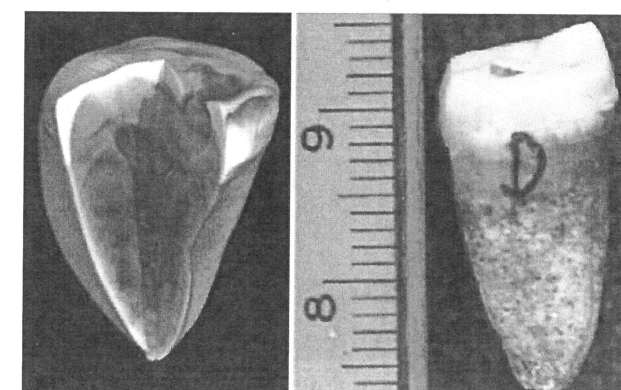


Fig. 52. Micro-CT of a Roman tooth.

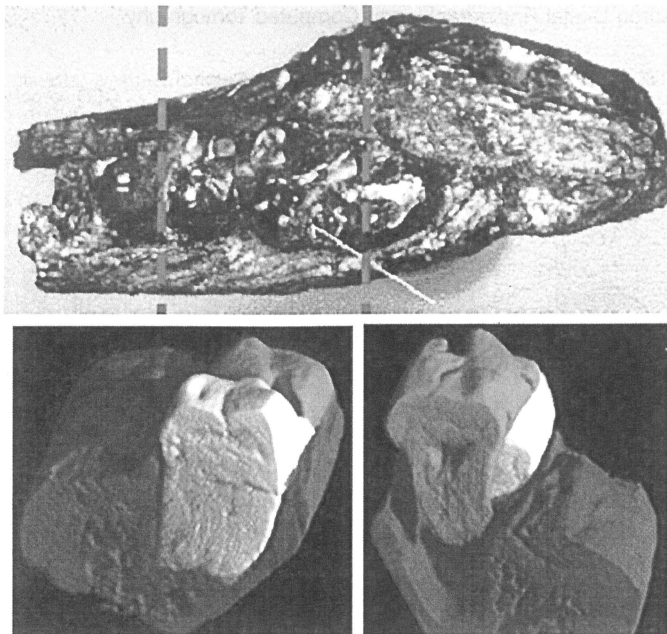


Fig. 53. Photo and micro-CT of a fossilised jaw.

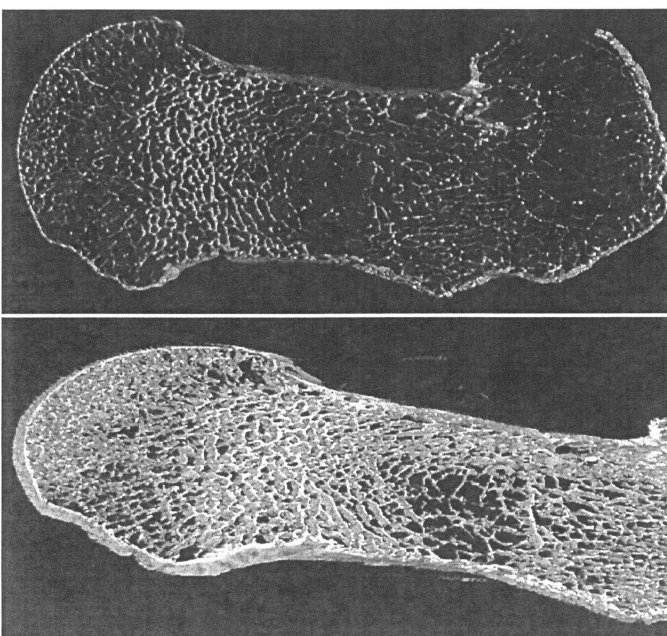


Fig. 54. CT of a human femur with a multi-slice detector (Fig. 38) and synchrotron light source.

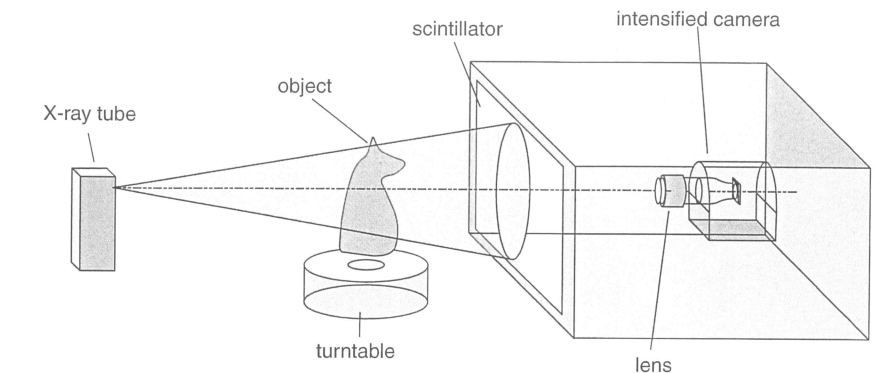


Fig. 55. An intensified camera collects the image produced by the X-rays on a scintillating material screen $30 \times 30 \text{ cm}^2$, that represents the radiographic projection of the object.

intensified, the images need very low radiation intensity. It is therefore possible to acquire objects very quickly or acquire thick objects (see Fig. 55). This CT system has been used for the inspection of a mummified Egyptian cat (see Fig. 56) (supplied by the Archaeological Museum of Bologna). Using suitable software, it is possible to “remove” the cat’s skeleton from its coffin (Fig. 57). This system operates well up to 300 kV.

9.3.2. Medium-high energy

This system is briefly described in Section 6.2. It has been tested by taking CT of objects of different shapes and compositions. Figures 58 to 60 show CT of a small bronze elephant, a wooden horse with an iron core and an ancient bronze head dating to Roman times. As the top part of the head is missing, the reconstructed image can also be visually



Fig. 56. Photo of an Egyptian coffin with a mummified cat (in collaboration with the Archaeological Museum of Bologna).

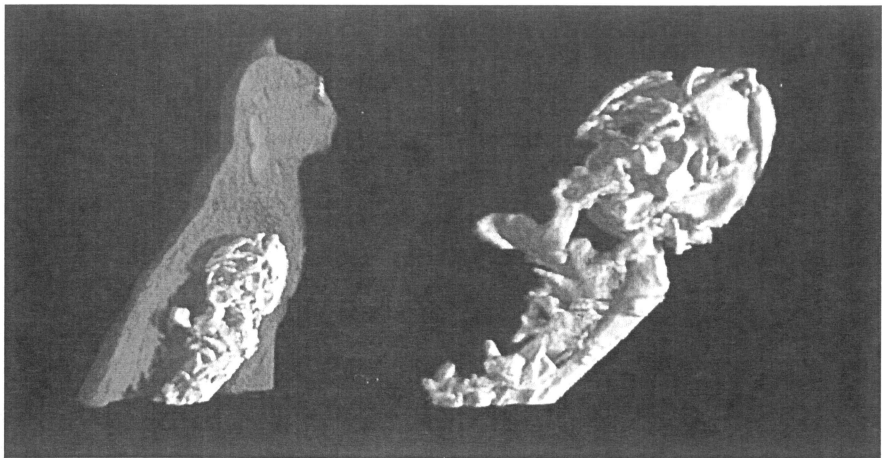


Fig. 57. CT of the coffin shown in Fig. 56 containing the skeleton of a cat.

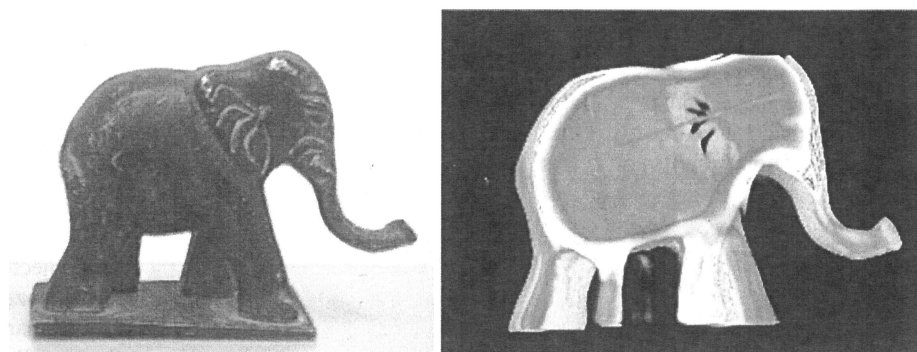


Fig. 58. CT of a small bronze elephant.

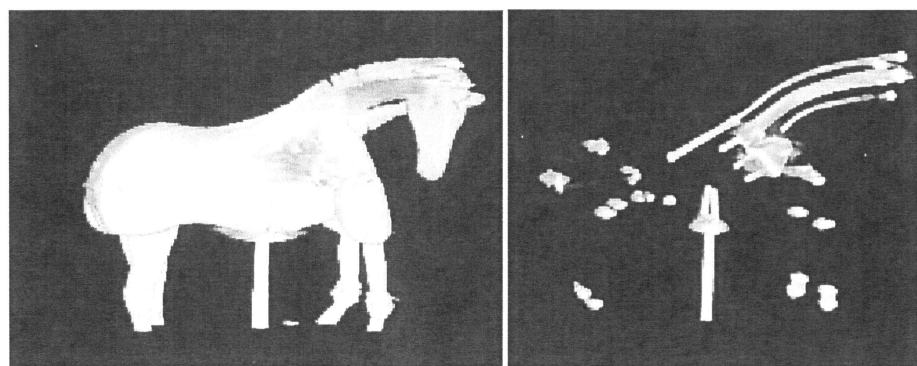


Fig. 59. CT of a wooden horse with iron core.

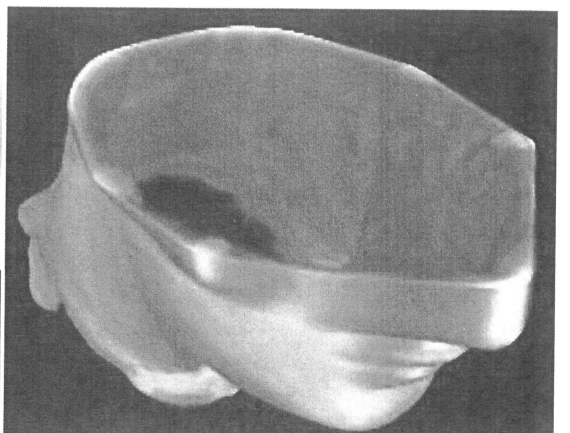


Fig. 60. A head of an ancient Roman bronze statue (see Fig. 44) and the 3D reconstruction thereof.

compared with the actual internal structure. This system can operate well up to 450 kV. Rather higher energy can be obtained by LINACs. With these X-ray sources metal objects can be inspected (for instance, see Refs. [11,40]).

Warning! Before irradiating a bronze statue (mainly for CT investigation), it is a good practice to keep part of the inner clay mould for conducting, the age measurement by thermo-luminescence technique. The irradiation, later on if desired by X-rays or γ rays would perturb the measurement, and the statue would appear older.

9.4. Computed tomography of a large ancient globe

In Palazzo Vecchio, at Florence, there is a large globe (2200 mm in diameter) created by a Dominican monk, Egnazio Danti, around 1567 (see Fig. 61). The Municipality of Florence, in collaboration with “Opificio delle Pietre Dure” in Florence,⁷ decided to set up an important diagnostic campaign for this wonderful masterpiece and repair, as much as possible, the injuries of time. Besides the cleaning of the surface, which had become brown, the project

⁷The diagnostic campaign was decided by the Municipality of Florence and by the “Opificio delle Pietre Dure” of Florence under the surveillance of “Soprintendenza per i Beni Architettonici e il Paesaggio” and for the “Patrimonio Storico Artistico e Demoantropologico” of the Provinces of Florence, Pistoia and Prato. The diagnostic campaign was carried out by the National Institute of Applied Optics (INOA) of Florence, the Institute of Science and Information Technology (ISTI-CNR) of Pisa, the Department of Physics of the University of Bologna, the Department of Chemistry of the University of Perugia, and the Systems Measurements Services (S.M.S.) at Sutri.

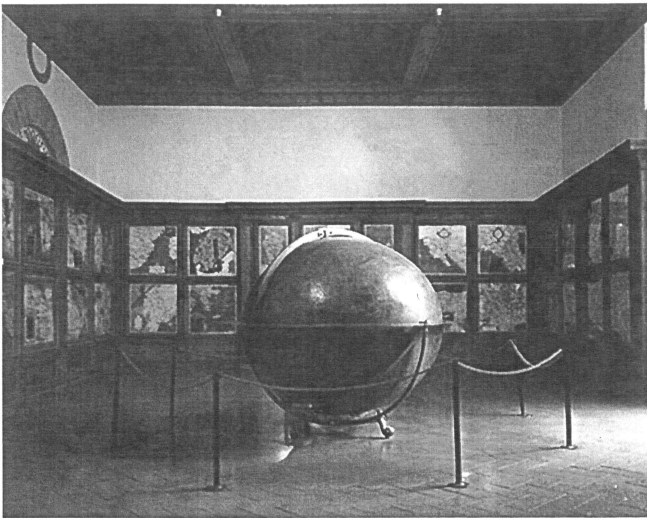


Fig. 61. The Map Room ("Sala delle Carte") with the old globe, in Palazzo Vecchio (Florence).

also involved an exploration of the nature and condition of its inner structure. It was therefore decided that in addition to the surface diagnosis, a CT scan would be performed. Our Department was assigned the task of performing this inspection. The difficulties of performing an *in-situ* CT scan of such a large object (maybe the largest ever subject to CT *in situ*) in a museum surrounded by visitors, were immediately evident. It was therefore necessary to perform the scan by night. If the "cone-beam" mode was chosen, the projection of the globe would ideally be on a screen with a surface area of $4 \times 4 \text{ m}^2$, located about 5 m from the X-ray source. With a planar detector, with dimensions of $30 \times 40 \text{ cm}^2$, about 33 000 images would be taken. In order to test the feasibility of performing the measurements, it was decided to take preliminary digital radiographs using a new type of fast EBCCD camera. This appliance, developed by the Russian firm Geosphaera, has a CCD with 528×286 pixels, a read-out time of 25 ms and a dynamic range of 12 bits. As the preliminary radiographs, taken in July 2003, gave good results, it was decided to proceed using the same system. The acquisition time, for one image, was of the order of 5 s. As a comparison, a normal radiograph using film took about 20 min for a distance of less than 3 m. In the detection system, shown in Fig. 62, the camera looks directly at the GOS scintillating screen; the 45° mirror is not necessary, as the X-ray intensity impinging on the camera at that distance (5 m) is very low. The globe (weighing about 1000 kg) was placed on a rotating platform. The set-up of the whole system is shown in Fig. 63. A motor moved the X-ray tube along an aluminium column. Two more motors moved the detector along the x - and y -axis.

In the case of the globe, it was not possible to perform CT in "cone beam" mode. In fact, taking into account the rule formulated in Section 8.2.5, (the angle of the cone must be

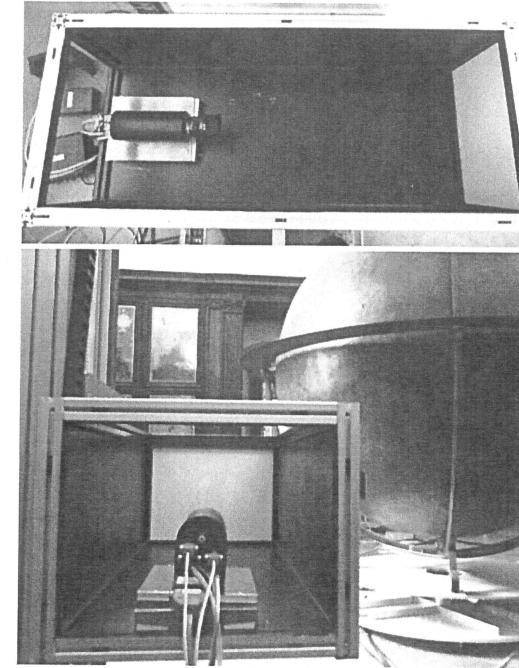


Fig. 62. The intensified TVcamera inside the box.

smaller than 10°), the X-ray source would be located too far from the detector. It was therefore decided to put the X-ray tube at different heights and to move the detector, aligned with the tube, in a horizontal direction only. In this way, we had 14 "cone beam" CTs but each one with a small angle, thus making it possible to apply the FDK approximation correctly.

To minimise the X-rays in the room and in the part of the globe not involved, the tube was equipped with a lead collimator. The preliminary radiographs showed that the internal structure was made of iron as reported in ancient documents written by Egnazio Danti. It was therefore necessary to adopt a portable 200 kV system (manufactured by Gilardoni S.P.A.). In order to pass through the iron structure and to minimise the artefacts, a voltage of 180 kV was used.

In short, the CT of this large globe was obtained thus:

- the X-ray tube was placed on the North Pole;
- the detector, located on the horizontal trail as shown in Fig. 63, was placed to the extreme right of the projection of the globe. At this point, an image was acquired;
- the platform, on which the globe was placed, was rotated in angular steps of 1° . After 360 acquisitions, the detector was translated by about 40 cm, then another 360 acquisitions were performed and so on, until the entire slice had been scanned;

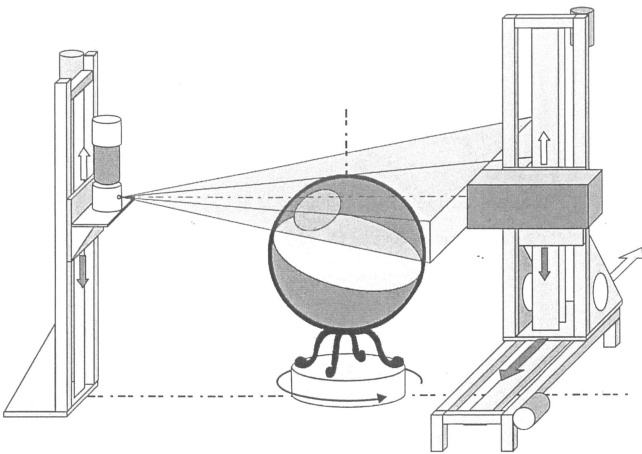


Fig. 63. Sketch of the system. The globe rotates over a platform with angular steps of 1° .

- (d) the tube was moved towards the South Pole and the operation was repeated, starting from point (b).

Each image was identified by three figures for slice, position of detector and angle. For a defined angle, these images were “welded” as shown in Fig. 64, corresponding to the slice No. 7 from the top. Figure 65 shows the different slices together. At this point, the 3D reconstruction was performed using appropriate software developed in our Department.

The inner structure, made of iron, then appeared as shown in Figs. 66 and 67. It was performed using a central pole, 8 bars as 2 tetrahedrons and 30 meridians. Using the segmentation of the image (see Section 4.3.3), it was possible to evaluate the volume of the iron inside, which weighed about 350 kg.

Ancient documents report that several pounds of hemp had been bought but it is not sure that the hemp was used in creating the globe. Probably it was put between the surface and the iron structure as shown by Fig. 68. The image is very noisy as the hemp is rather transparent to X-rays of the energy used. The measurements took about one month (June 2004) to complete and were performed by young researchers and PhD students (in Physics and Computer Science) at the University of Bologna (Fig. 69).



Fig. 64. One of the fourteen slices obtained.

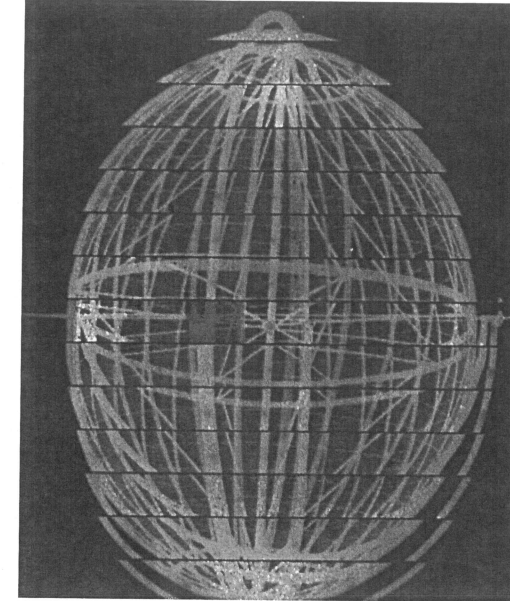


Fig. 65. All 14 slices together.

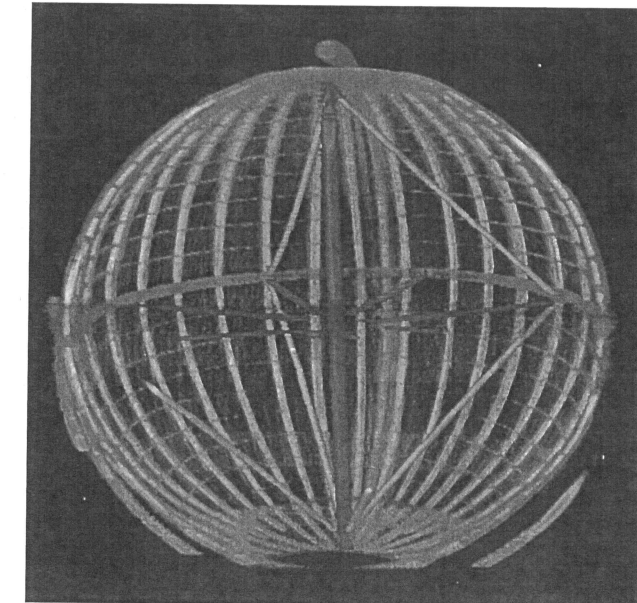


Fig. 66. A three-dimensional reconstruction.

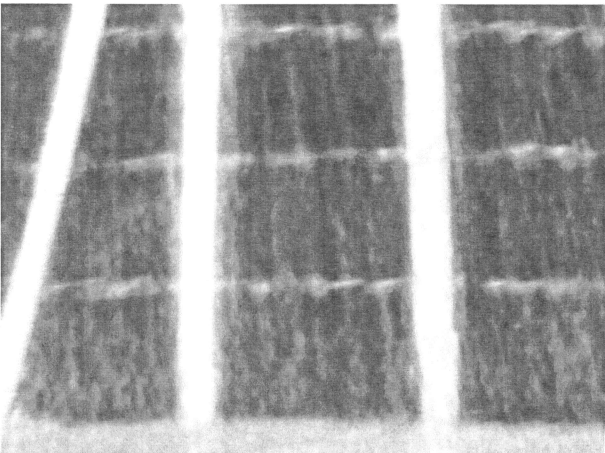


Fig. 68. This image shows a material that could be hemp chord.

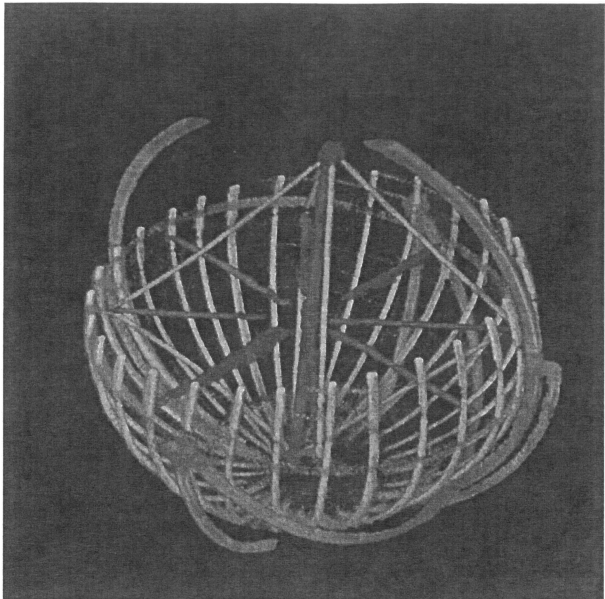


Fig. 67. An exploded 3D reconstruction.

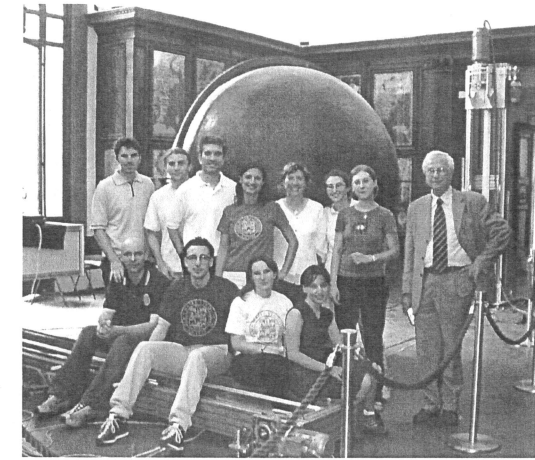


Fig. 69. The team of young researchers and PhD students (physicists and computer scientists) with the author, at the end of the measurement phase. From left to right, they are: (stand up) Alessandro Pasini, Nico Lanconelli, Matteo Bettuzzi, Samantha Cornacchia, Maria Pia Morigi, Marilisa Giordano, Alice Miceli, the author; (sit down) Alessandro Fabbri, Davide Bianconi, Carlotta Cucchi, Emilia di Nicola. Not in picture: Davide Romani, Alberto Rossi, Rossella Brancaccio.

9.5. Neutron tomography

Generally speaking, neutron tomography is performed using thermal neutron beams produced by nuclear reactors [29] or by suitable facilities [42]. Less frequently, cold [43] and fast neutrons are also used [44].

In general, the beams have a circular section and are of the parallel type (like synchrotron light). Acquisition is performed by planar detectors based on ^6Li and ZnS [28]. Neutron DRs and CTs of a model of a small helmet and of an ancient amulet (cat) are reported in Fig. 70 [45]. Where possible, it is very interesting to compare (or overlap) DRs and CTs performed using X-rays (or γ rays) and those using neutrons [46].

9.6. Induced activation by X-rays and neutrons

9.6.1. Activation by X-rays

When high-energy photons interact with atomic nuclei, there is the possibility that the struck nucleus will emit a neutron that, in turn, makes the surrounding materials radioactive. Each nucleus has a threshold energy for this photoreaction, below which the neutron is not emitted. The smallest threshold energy is 1.6 MeV, for ^9Be , then 2.2 MeV for ^2H , therefore if one uses radioisotopic sources like ^{60}Co or ^{135}Cs , which emit photons with lower energies, it is physically impossible for the irradiated materials to become radioactive.

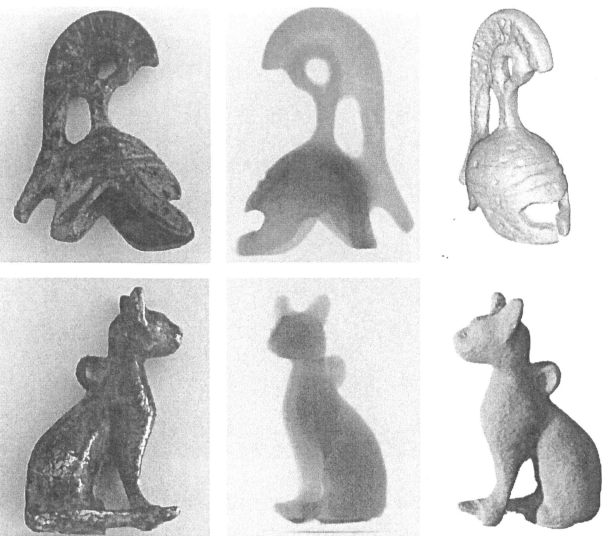


Fig. 70. Photos, neutron radiographies and neutron tomographies of a model of a small helmet and of an ancient amulet (cat).

On the contrary, if one uses LINACs as a photon source (see Section 2.3.2), the emission of neutrons is possible, especially if heavy materials, like lead, are irradiated. The threshold energy for Pb is about 7 MeV. In practice, for LINACs with energy less than 10 MeV, induced radioactivity is rather small, almost negligible.

9.6.2. Activation by neutrons

Apart from the difficulty of obtaining neutrons, the main problem of neutron radiography or tomography is that the sample becomes radioactive. The induced radioactivity can be so high that for some tests (*e.g.* real time radioscopy with high neutron fluxes), the sample cannot be handled for many days or months.

Warning! When high energy LINACs or neutrons are used as radiation source, always refer to an expert in radiation protection.

This recommendation is also valid when “in the field” measurements are performed, whatever the source.

10. SUGGESTIONS AND CONCLUSIONS

An increase in scientists’ interest in cultural heritage and decrease in humanists’ suspicion of technology have overcome an age-old debate in understanding the works of art. After all, were not Leonardo and Michelangelo, both scientists and artists? Many new applications

based on physical techniques are being developed. In this chapter, we have provided some basic information on digital radiography and computed tomography without the presumption to be exhaustive. It should however be pointed out that the CT field is a very difficult one. The ease with which CT can be performed in the medical field may prove deceptive: medical CT was designed for the human body (composed mainly of water) alone and cannot be successfully used on bodies with different shapes or compositions. In order to perform good, non-destructive evaluations, the most suitable DR or CT system (source, moving equipment, detector and elaboration software) must be carefully chosen to avoid obtaining disappointing results, wasting time and money and ... losing faith in Physics.

APPENDIX A: BASIC NOTIONS CONCERNING FOURIER TRANSFORMS

A.1. The Fourier series

This appendix contains some of the basic concepts used in the imaging field.

The Fourier transform can be considered as an extension of the development in Fourier series that, for a periodic function of period T , has the following expression:

$$f(t) = \frac{1}{2} a_0 + \sum_{n=1}^{\infty} \left(a_n \cos \frac{2\pi}{T} nt + b_n \sin \frac{2\pi}{T} nt \right) \quad (\text{A.1})$$

where a_0 , a_n and b_n are expressed by:

$$\begin{aligned} a_0 &= \frac{2}{T} \int_{-T/2}^{T/2} f(t) dt, \\ a_n &= \frac{2}{T} \int_{-T/2}^{T/2} f(t) \cos \frac{2\pi}{T} nt dt, \\ b_n &= \frac{2}{T} \int_{-T/2}^{T/2} f(t) \sin \frac{2\pi}{T} nt dt. \end{aligned} \quad (\text{A.2})$$

If $f(t)$ is a symmetric function, only the terms a_0 and a_n are not equal to zero.

Figure A.1(A) shows a sinusoidal signal affected by noise. By developing this function into a Fourier series and taking the fundamental harmonic only, the noise, that is the remaining part of the series, is removed (Fig. A.1(B)). Conversely, by taking all harmonics with $n > 1$, one retains the noise and discards the regular shape of the signal (Fig. A.1(C)).

With a simple algebraic operation, making use of Euler’s formula:

$$e^{jt} = \cos t + j \sin t, \quad (\text{A.3})$$

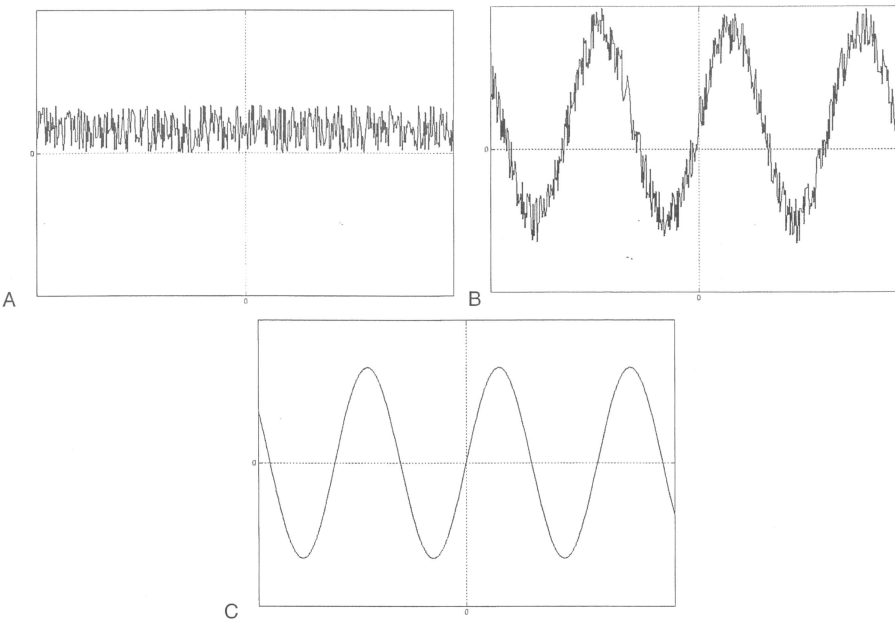


Fig. A.1. (A) A sinusoidal function with a superimposed noise; (B) only fundamental harmonic is retained; (C) the noise (difference between the whole signal and the fundamental harmonic).

the equations (A.1) and (A.2) assume the form:

$$f(t) = \sum_{n=-\infty}^{+\infty} c_n \exp\left(j \frac{2\pi}{T} nt\right), \quad (\text{A.4})$$

where:

$$c_n = \frac{1}{T} \int_{t_0}^{t_0+T} f(t) \exp\left(-j \frac{2\pi}{T} nt\right) dt. \quad (\text{A.5})$$

One important relation is:

$$\frac{1}{2\pi} \int_{-\pi}^{+\pi} \{f(t)\}^2 dt = \sum_{-\infty}^{+\infty} |c_n|^2.$$

The totality of a_0, a_n, b_n or c_n where, $n = 1, 2, \dots, \infty$, is defined as the “spectrum” of that function. Giving the infinite values constituting the spectrum is equivalent to giving the infinite values of the function $f(t)$ for each point of the interval $(0, T)$.

A.2. One-dimensional Fourier transform

It is possible to demonstrate that, by extending the integration limits from $-\infty$ to $+\infty$ and proceeding as in the discretised case, equations (A.4) and (A.5) are transformed into:

$$f(x) = \int_{-\infty}^{+\infty} F(u) e^{j2\pi ux} du, \quad (\text{A.6})$$

$$F(u) = \int_{-\infty}^{+\infty} f(x) e^{-j2\pi ux} dx. \quad (\text{A.7})$$

$F(u)$ is known as the *Fourier Transform* of $f(x)$ and is equivalent to the aforementioned spectrum. The two equations comprise the *Fourier Transform pair*.

$f(x)$, which can be obtained by $F(u)$, is also known as the *inverse Fourier Transform*.

In general, the transformed function is a complex function, for which one can use the usual notation for complex numbers:

$$F(u) = R(u) + jI(u), \quad (\text{A.8})$$

or in the exponential form, making use of Euler's relation:

$$F(u) = |F(u)| \cdot e^{j\Phi(u)}, \quad (\text{A.9})$$

where:

$$|F(u)| = \{R(u)^2 + I(u)^2\}^{1/2} \quad (\text{A.10})$$

is denominated the magnitude or spectrum of the Fourier Transform and

$$\Phi(u) = \tan^{-1} \frac{I(u)}{R(u)} \quad (\text{A.11})$$

is the *phase angle*.

The square of the modulus:

$$E(u) = |F(u)|^2 = R(u)^2 + I(u)^2 \quad (\text{A.12})$$

is known as the energy spectrum or power spectrum of $f(x)$.

A *Fourier pair*, with

$$f(x) = \begin{cases} a & 0 \leq x \leq x_0 \\ 0 & \text{otherwise} \end{cases}$$

is shown in Fig. A.2. It should be remembered that $I(u)$, $R(u)$ and $|F(u)|$ extend to infinity, even if $f(x)$ differs from zero in a finite interval.

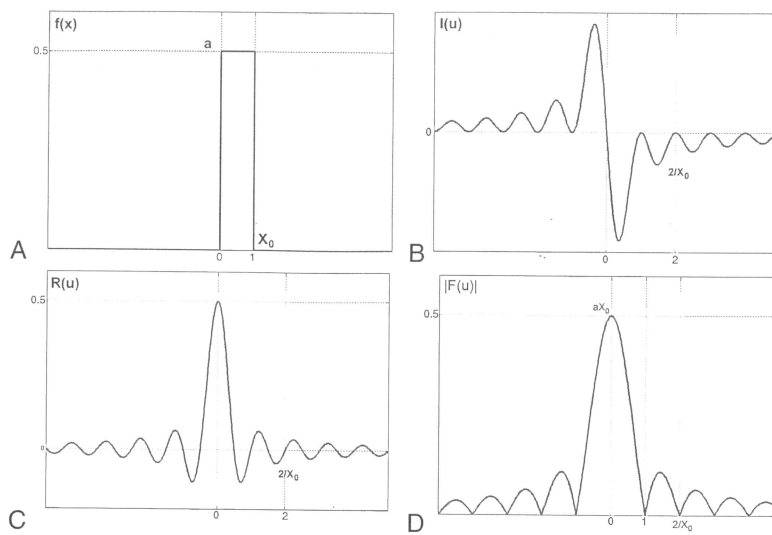


Fig. A.2. (A) $f(x)$, Rectangular function; (B) $I(u)$, imaginary component of $F(u)$; (C) $R(u)$, real component of $F(u)$; (D) spectrum of $F(u)$.

A.3. Two-dimensional Fourier transform

The extension to two variables, u and v , gives:

$$F(u, v) = \int_{-\infty}^{+\infty} \int_{-\infty}^{+\infty} f(x, y) e^{-j2\pi(ux+vy)} dx dy, \quad (\text{A.13})$$

for the transform and

$$f(x, y) = \int_{-\infty}^{+\infty} \int_{-\infty}^{+\infty} F(u, v) e^{j2\pi(ux+vy)} du dv, \quad (\text{A.14})$$

for the inverse transform.

Once again, in two-dimensional cases, the transformed function is a complex one. Using the notation for complex numbers:

$$F(u, v) = R(u, v) + jI(u, v), \quad (\text{A.15})$$

or, making use of Euler's relation in exponential form:

$$F(u, v) = |F(u, v)| \cdot \exp(j\Phi(u, v)), \quad (\text{A.16})$$

where:

$$|F(u, v)| = \{R(u, v)^2 + I(u, v)^2\}^{1/2}, \quad (\text{A.17})$$

and

$$\Phi(u, v) = \tan^{-1} \frac{I(u, v)}{R(u, v)}, \quad (\text{A.18})$$

with the same notation as in the mono-dimensional case.

A.4. One-dimensional discrete Fourier transform

Because we are interested in processing digital images, which are equivalent to numerical matrices, equations (A.13) and (A.14) must be rewritten for discrete functions [18].

Starting from a one-dimensional discrete function, $f(x)$, $x = 0, 1, 2, \dots, N - 1$, the *discrete Fourier Transform* (DFT) is:

$$F(l) = \frac{1}{N} \sum_{n=0}^{N-1} f(n) \exp \left[-j2\pi \frac{nl}{N} \right], \quad l = 0, 1, \dots, N - 1 \quad (\text{A.19})$$

computed for values of $u = 0, 1, 2, \dots, N - 1$.

As we are dealing with digital images, we have assumed the sampling intervals to be constant, and because we started with a sampled function, its transform is also sampled. The definition intervals have been properly normalised so that the total interval is equal to 1.

The inverse transform, is:

$$f(k) = \sum_{l=0}^{N-1} F(l) \exp \left[\frac{j2\pi kl}{N} \right], \quad k = 0, 1, \dots, N - 1 \quad (\text{A.20})$$

The correspondence of the two transforms is immediately demonstrated by substituting (A.20) with (A.19) or *vice versa*.

A.5. Two-dimensional discrete Fourier transform

The extension of DFT in two-dimensions is fairly straightforward. The DFT of a two-dimensional function $f(x, y)$ (far more interesting with regard to digital image processing) with a size of $M \times N$ is given by the equation:

$$F(k, l) = \frac{1}{NM} \sum_{m=0}^{M-1} \sum_{n=0}^{N-1} f(m, n) \exp \left[-j2\pi \left(\frac{km}{M} + \frac{ln}{N} \right) \right], \quad (\text{A.21})$$

$$k = 0, 1, \dots, M - 1; l = 0, 1, \dots, N - 1.$$

Similarly:

$$f(m, n) = \sum_{k=0}^{M-1} \sum_{l=0}^{N-1} F(k, l) \exp \left[j2\pi \left(\frac{km}{M} + \frac{ln}{N} \right) \right], \quad (\text{A.22})$$

$$m = 0, 1, \dots, M-1; n = 0, 1, \dots, N-1$$

Equations (A.21) and (A.22) are written for rectangular matrices $M \times N$, and comprise the *two-dimensional, discrete Fourier Transform (DFT) pair*.

For square matrices $N \times N$, these equations can be rewritten as:

$$F(k, l) = \frac{1}{N} \sum_{m=0}^{N-1} \sum_{n=0}^{N-1} f(m, n) \exp \left[-j2\pi \left(\frac{km + ln}{N} \right) \right], \quad (\text{A.23})$$

$$k = 0, 1, \dots, N-1; l = 0, 1, \dots, N-1$$

Similarly:

$$f(m, n) = \sum_{k=0}^{N-1} \sum_{l=0}^{N-1} F(k, l) \exp \left[j2\pi \left(\frac{km + ln}{N} \right) \right], \quad (\text{A.24})$$

$$m = 0, 1, \dots, N-1; n = 0, 1, \dots, N-1$$

The calculation for the spectrum, the phase and the energy spectrum is performed as seen in the continuum.

If N is a power of 2 (*i.e.* $N = 2^n$), the calculation time of $F(k, j)$ and $f(m, n)$ is drastically reduced (of a factor $N/\log_2 N$) by using an algorithm known as the *Fast Fourier Transform (FFT)* [17]. The FFT algorithm is normally used in digital image processing.

A.6. Some properties of 2D discrete Fourier transforms

Mean value

Let us consider the discrete function $f(x, y)$. Its mean value is given by

$$\bar{f} = \frac{1}{N^2} \sum_{m=0}^{N-1} \sum_{n=0}^{N-1} f(m, n). \quad (\text{A.25})$$

Moreover, for $k = l = 0$, equation (A.23) becomes

$$F(0, 0) = \frac{1}{N} \sum_{m=0}^{N-1} \sum_{n=0}^{N-1} f(m, n). \quad (\text{A.26})$$

We can conclude that

$$\bar{f} = \frac{1}{N} F(0, 0) \quad (\text{A.27})$$

which shows us that the term $F(0,0)$ corresponds to N -times the average grey level of the image.

Periodicity and symmetry

From equation (A.23), one can easily show that:

$$F(k, l) = F(k + N, l) = F(k, l + N) = F(k + N, l + N) \quad (\text{A.28})$$

The same occurs for $f(x, y)$ in the spatial domain. This peculiarity highlights the fact that the *Fourier Transform* and its inverse repeats indefinitely in both spatial dimensions.

It is not difficult to demonstrate that

$$[f(x, y)(-1)^{x+y}] = F(u - N/2, v - N/2) \quad (\text{A.29})$$

This relation states that the origin of the *Fourier Transform* of $f(x,y)(-1)^{x+y}$, that is $F(0,0)$, is at $u = N/2$ and $v = N/2$. The translation of the origin gives a better representation of $F(u,v)$, as shown in Fig. A.3.

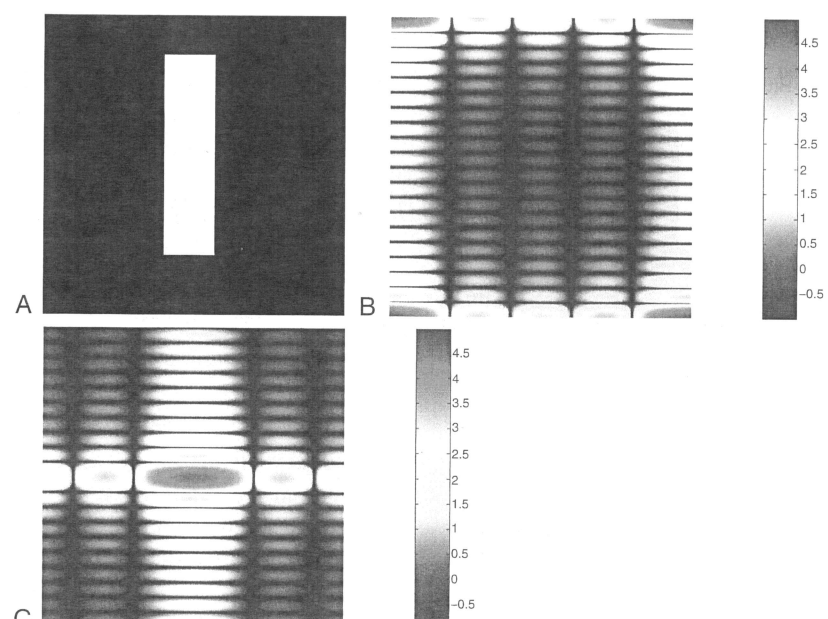


Fig. A.3. (A) Image; (B) Fourier Transform of (A) with the origin in $(0,0)$; (C) Fourier Transform of (A) with origin in $(N/2, N/2)$.

There are also other interesting properties, such as:

$$F(k, l) = F^*(-k, -l), \quad (\text{A.30})$$

where F^* is the complex conjugate of F . Passing to absolute values:

$$|F(k, l)| = |F(-k, -l)|. \quad (\text{A.31})$$

A.7. Filtering in the frequency domain

Figure A.1 shows that, given a signal and its spectrum, the slowly varying components of the signal are related to the low frequencies in the spectrum. Conversely, the rapidly varying components (*e.g.* the “noise”) refer to the high frequencies. By filtering the high frequencies, we can “clean” the signal. The same happens for an image (signal) and its *Fourier Transform* (spectrum). We can decrease the noise by decreasing the importance of the high frequencies (*lowpass filtering*) or enhance the contrast by decreasing the importance of the low frequencies (*highpass filtering*). The filtering is performed by multiplying $F(u, v)$ by a function $H(u, v)$, named *filter transfer function*, which decreases certain frequencies and leaves the others unchanged. Some shapes of $H(u, v)$ are shown in Fig. A.4.

Fourier domain filtering is performed as follows:

(a) acquire the image $f(x, y)$ and perform all possible pre-processing (*e.g.* subtract noise);

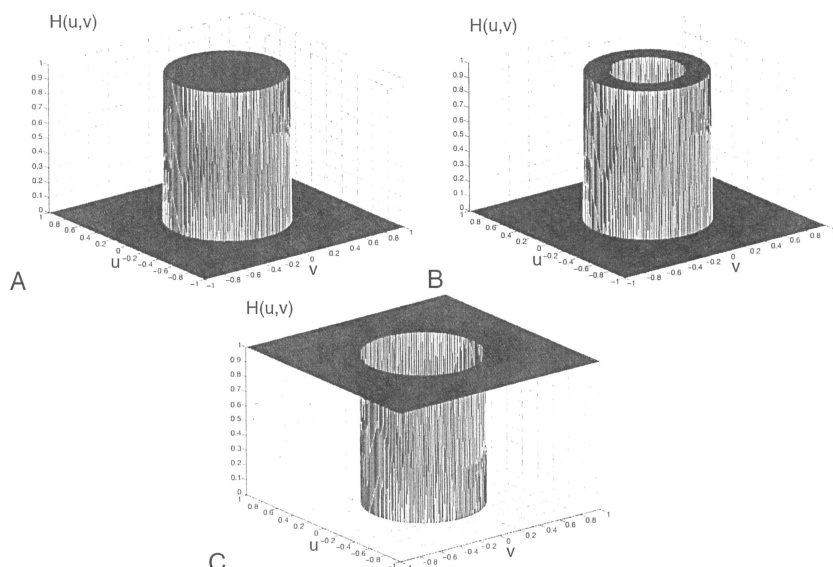


Fig. A.4. Some shapes of the filter function $H(u, v)$. (A) “Ideal” low-pass filter; (B) “Ideal” selecting band filter; (C) “Ideal” high-pass filter.

- (b) centre $F(u, v)$, multiplying $f(x, y)$ by $(-1)^{x+y}$, as indicated in equation (A.29);
- (c) compute $F(u, v)$ of the image;
- (d) multiply $F(u, v)$ by the filter function $H(u, v)$;
- (e) compute the inverse DFT of $G(u, v) = H(u, v) F(u, v)$;
- (f) multiply the real part of the Filtered Image $F^{-1}[G(u, v)]$ by $(-1)^{x+y}$.

It should be pointed out that with this procedure we enhance the image as a whole; it is not a “local treatment”.

A.8. Convolution of two functions

The convolution of two functions is a very important operation for image restoration. The “local treatment” can be traced back to a convolution of a function (*the image*) with another function (*the mask* or *the filter*).

The convolution of two functions $f(x)$ and $h(x)$, formally stated as $f(x) * h(x)$, is defined by the integral:

$$g(x) = f(x) * h(x) = \int_{-\infty}^{+\infty} f(\xi)h(x - \xi)d\xi. \quad (\text{A.32})$$

One important case is when $h(x)$ is the delta function $\delta(x)$ (Dirac function or pulse function), which has the following properties:

$$\int_{-\infty}^{+\infty} f(x)\delta(x - x_0)dx = f(x_0), \quad (\text{A.33a})$$

$$\int_{-\infty}^{+\infty} \delta(x - x_0)dx = \int_{x_0 - \varepsilon}^{x_0 + \varepsilon} \delta(x - x_0)dx = 1. \quad (\text{A.33b})$$

Using equation (A.26), it is easy to demonstrate that the convolution of any function with a delta function gives a function that is a translated copy of the original function. The extension to two-dimensional functions is straightforward.

Convolution Theorem

The main importance of the convolution operation is connected to the “Convolution Theorem”. If $f(x, y)$ and $h(x, y)$ have the functions $F(u, v)$ and $H(u, v)$ as Fourier transforms respectively, the first part of the convolution theorem states that $f(x, y) * h(x, y)$ has the function $F(u, v) \cdot H(u, v)$ as a Fourier transform. These results can be formally presented as:

$$f(x, y) * h(x, y) \Leftrightarrow F(u, v) \cdot H(u, v). \quad (\text{A.34})$$

The double arrows (\Leftrightarrow) indicate that the convolution of $f(x, y)$ with $h(x, y)$ can be obtained by the Fourier transforms of $f(x, y)$ and, $h(x, y)$, performing the multiplication

element-by-element (or pixel by pixel) of F and H , then taking the inverse Fourier transform of the function-product obtained.

Calculating a convolution integral using the procedure outlined above is much faster than a direct calculation.

Equation (A.34) can also be written in the form:

$$f(x, y) \cdot h(x, y) \Leftrightarrow F(u, v) * H(u, v), \quad (\text{A.35})$$

which states that the convolution in the frequency domain is equivalent to a multiplication in the spatial domain.

APPENDIX B: MODULATION TRANSFER FUNCTION

B.1. Point spread function, line spread function and edge spread function

Another important application of the Fourier transform is the determination of the modulation transfer function (MTF). The MTF is the principal function that quantifies the spatial resolution of an image-acquiring system.

Let us perform a simple experiment. Take a well-focused overhead projector and place a piece of cardboard with a sharp edge over it. If we now look at the projected image, we realise that it has a black-and-white distribution, like a “step function”, as shown in Fig. B.1(A). If we move the cardboard away, the edge becomes less sharp; it will no longer be a step function but something similar to that shown in Fig. B.1(B).

There will be a “spread” on the boundary: we have produced an “edge spread function” (ESF). The blurring will depend on the distance of the cardboard from the overhead

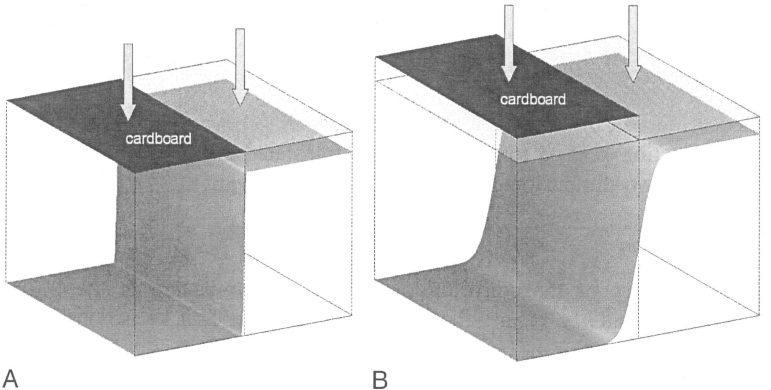


Fig. B.1. A cardboard, with a sharp edge, is put over a well-focused overhead projector plane. The image produced is a black-and-white image as a “step function” (curve (A)). The cardboard is then moved away and the grey distribution is similar to a step function but not so sharp like in the former case (curve (B)). The step function is affected by “blurring”.

projector plane. The same will happen if we have a small slit in the cardboard. When the entire system is well focused, the grey distribution produced is like a narrow “rectangular function”, which can be approximated with a mono-dimensional Dirac delta function, $\delta(x - x_0)$. By moving the cardboard away as described above, we obtain the image shown in Fig. B.2 (like a Gaussian). We have done the so-called “line spread function” (LSF). As an extension of this, a small hole can be represented as a 2D delta function, $\delta(r - r_0)$, and the unfocused one will be the “point spread function” (PSF) (Fig. B.3). This means that an input “point signal” undergoes a sort of 2D gaussian blurring, given by the shape (width) of the PSF.

Now let us consider a well-collimated linear beam of photons or neutrons, such as that obtained from a synchrotron or collimator in a nuclear reactor. Let these particles pass through a thin slit, which we consider as $\delta(x - x_0)$, and impinge on a scintillating screen. A flash of light will be produced isotropically in the point where an interaction with the scintillating material occurs: for instance, at a depth z from the screen face where the image is formed. The light will escape the screen within a broad angle so that the spatial distribution of the escaped light, $L(x - x_0)$,⁸ will have the shape of an LSF. The nearer the image plane, the sharper the LSF. It is possible to demonstrate that [47]:

$$L(x - x_0) = \left[\frac{\lambda/\pi}{1 + \lambda^2(x - x_0)^2} \right], \quad (\text{B.1})$$

where $\lambda = z^{-1}$ (λ is called “resolution parameter”).

The maximum of this function occurs for $x = x_0$

$$L(x = x_0) = \frac{\lambda}{\pi}. \quad (\text{B.2})$$

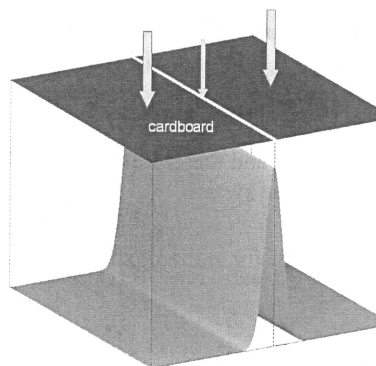


Fig. B.2. A cardboard, with a thin slit, is put over a well-focused overhead projector plane. The grey distribution is a narrow “rectangular function”, like a mono-dimensional Dirac delta function. The cardboard is then moved away and the grey distribution becomes similar to a Gaussian. We have obtained the so-called “line spread function”.

⁸ The right term for equation B.1 is the so-called “Lorentzian” function (see Mathworld.wolfram.com) and, in general, it appears when resonance phenomena are dealt with.

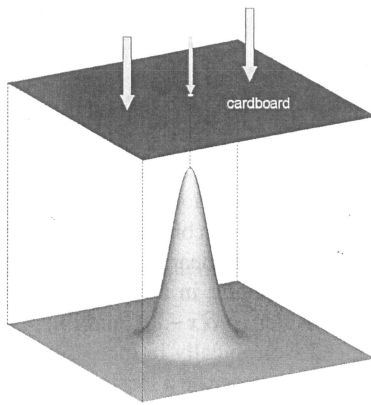


Fig. B.3. A cardboard, with a small hole, is put over a well-focused overhead projector plane. The grey distribution is like a two-dimensional Dirac delta function. The cardboard is then moved away and the grey distribution becomes similar to a Gaussian. Thus we have obtained the so-called “point spread function”.

The width at which $L(x - x_0)$ assumes half of its maximum value is defined as “full width at half maximum” (FWHM) (see Fig. B.4)

$$\frac{1}{2} \left(\frac{\lambda}{\pi} \right) = \frac{\lambda/\pi}{1 + \lambda^2 x_{1/2}^2} \quad (\text{B.3})$$

so that the

$$\text{FWHM} = \frac{2}{\lambda} \quad (\text{B.4})$$

Low FWHM means high resolution and therefore the FWHM is sometimes assumed as an index of the spatial resolution of the system.⁹

⁹ As x_0 is an arbitrary value, we can put $x_0 = 0$, and equation (B.1) becomes:

$$L(x) = \left[\frac{\lambda/\pi}{1 + \lambda^2 x^2} \right] \quad (\text{i})$$

When other factors exist that degrade the LSF (such as background and noise), they are combined and then equation (i) is assumed to be of a gaussian type:

$$L(x) = \frac{\alpha}{\sqrt{\pi}} \exp(-\alpha^2 x^2), \quad (\text{ii})$$

where α is called the “resolution parameter”.

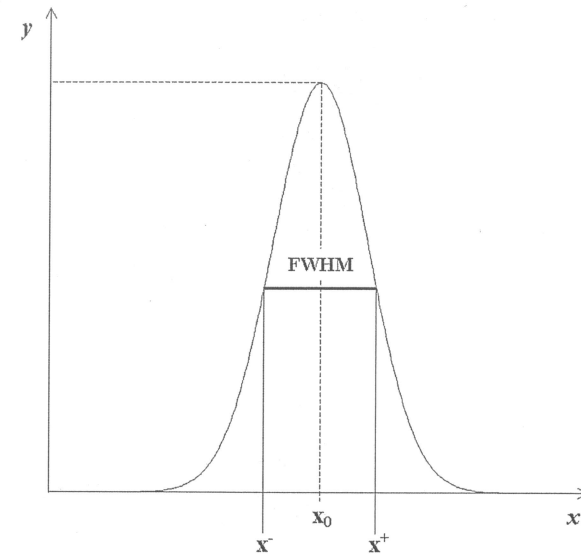


Fig. B.4. At the values x^- and x^+ , the function has half of its maximum value. The Full Width at Half Maximum (FWHM), $(x^+ - x^-)$, is equal to $2/\lambda$, an index of the spatial resolution of the system.

The edge spread function, $S(x)$, can be intended as a superposition of infinite line spread functions. This can be obtained by integrating $L(x - x_0)$ up to $+\infty$:

$$S(x) = N \int_0^{\infty} L(x - x_0) dx_0, \quad (\text{B.5})$$

where N is a normalisation parameter.

By substituting $L(x - x_0)$ with its expression, given by equation B.1, we have:

$$S(x) = N \int_0^{\infty} \left(\frac{\lambda/\pi}{1 + \lambda^2(x - x_0)} \right) dx_0. \quad (\text{B.6})$$

With the position $t = (x_0 - x)\lambda$, the integral assumes the following shape:

$$S(x) = \frac{N}{\pi} \int_{-\lambda x}^{+\infty} \left(\frac{dt}{1 + t^2} \right) = \frac{N}{\pi} [\arctg(t)]_{-\lambda x}^{+\infty} = \frac{N}{\pi} \left[\frac{\pi}{2} - \arctg(-\lambda x) \right], \quad (\text{B.7})$$

which, finally, gives the edge spread function (ESF):

$$S(x) = N \left[\frac{1}{2} + \frac{1}{\pi} \operatorname{arctg}(\lambda x) \right]. \quad (\text{B.8})$$

Conversely, the differentiation of the ESF gives the LSF. As it is easier to measure the ESF than the LSF, we will obtain the MTF by measuring the ESF, as demonstrate below.

For instance, if the measured function is the optical density of a film, $D(x)$, it can be represented as the superposition of the real signal, noise and the background (see Fig. B.5):

$$D(x) = D_0(x) + D_n + D_b \quad (\text{B.9})$$

where:

$D_0(x)$ = component associated with the recording system;

D_n = component associated with the statistical noise (*e.g.* granular composition of the film);

D_b = optical density associated with the film not directly exposed to the radiation.

It is possible to infer the λ of the system by fitting the function $D(x)$ by the expression on the right hand side of equation (B.8). The FWHM is then obtained by equation (B.4).

Another simpler way to obtain the FWHM is as given below:

For $x = \lambda^{-1}$, we get

$$D(\lambda^{-1}) = D(\lambda^{-1}) = \frac{1}{2} + \frac{1}{\pi} \operatorname{arctg}(\lambda \lambda^{-1}) = \frac{1}{2} + \frac{1}{\pi} \frac{\pi}{4} = \frac{3}{4} = 0.75,$$

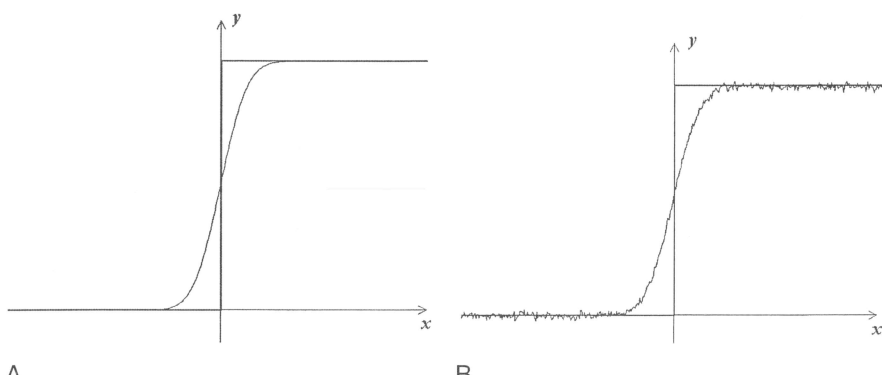


Fig. B.5. The measured distribution of an ESF affected by noise.

and for $x = -\lambda^{-1}$

$$D(-\lambda^{-1}) = \frac{1}{2} - \frac{1}{\pi} \operatorname{arctg}(-1) = \frac{1}{2} - \frac{1}{4} = \frac{3}{4} = 0.25,$$

so that, having measured the ESF, its 75% corresponds to $x_1 = 1/\lambda$ and its 25% corresponds to $x_2 = -1/\lambda$. Their difference, $(x_1 - x_2) = 2/\lambda = \text{FWHM}$.

We can conclude that by measuring ESF, it is possible to obtain the FWHM related to the spatial resolution of the acquisition system.

B.2. Optical Transfer Function and Modulation Transfer Function

Introduction

If we have a “step function” as the “input function” of a system, we will have a smoother curve as the “output function”. In other words, if we have an input function $f_i(x_0)$, given by:

$$f_i(x_0) = \begin{cases} 0 & \text{for } -\infty < x < x_0, \\ 1 & \text{for } x \geq x_0 \end{cases}, \quad (\text{B.10})$$

the output function, $g(x)$, will be the convolution of $f_i(x_0)$ with the LSF, $L(x - x_0)$:

$$g(x) = N \int_{-\infty}^{+\infty} f_i(x_0) L(x - x_0) dx_0 = f_i(x_0) * L(x). \quad (\text{B.11})$$

From the “convolution theorem” (see Appendix A, equation (A.34) applied to one-dimensional functions, one can obtain:

$$f_i(x) * L(x) \Leftrightarrow F(u) \cdot H(u) \quad (\text{B.12})$$

where function $H(u)$ is the Optical Transfer Function (OTF) of the system, as will be explained later in Section B.4. Its modulus, $|H(u)|$, is defined as the Modulation Transfer Function (MTF) of the system.

In this case (one-dimensional geometry), the MTF is the modulus of the Fourier Transform of the Line Spread Function.

B.3. Measurement of the Modulation Transfer Function for a linear system

There are several ways of measuring the MTF of a system. Here we give some indications of how to proceed for the MTF of a digital camera.

The starting point consists in the issues explained above, *i.e.* the modulus of the Fourier Transform of the LSF of a system is the MTF. In our case, the LSF can be obtained by differentiating the ESF. The main problem is therefore measuring the ESF as accurately as possible.

One can use the following procedures.

- Keep an image of an edge by the camera. Be sure that the edge is very sharp and the material is almost black to the radiation used (An edge that is good for low energy X-rays is not usually a good edge for X-rays produced by a LINAC).¹⁰
- Extract numerical data corresponding to a line crossing the edge perpendicularly.
- Correct for the noise due to background and CCD defects.
- Differentiate the obtained curve to get the LSF. (Some researchers prefer to fit the obtained LSF with a Gaussian, then to perform the FFT of the Gaussian obtained by the fit).
- Calculate the modulus of the Fast Fourier Transform of the LSF to obtain the MTF.

It has to be remembered that what we measure is the MTF of the system. In this case: the defects of the CCD sensor, the lens aberration, the diffused component of the radiation, the “penumbra” caused by the non-punctiform focal spot of the X-ray tube, and so on, are combined.

However, the calculation of the MTF function from experimental data requires a deeper knowledge of the discrete implementation of the Fourier Transform and its output. This is not dealt with herein; for a detailed description of the discrete Fourier transform and the calculation of the MTF by means of the edge technique, see works by Kak and Slaney [32] and Fujita *et al.* [48].

B.4. Modulation Transfer Function: general definition

Let us assume that we want to reproduce an object, which can be described as a function $I(x_0, y_0)$ in the object plane, represented by the subindex “0”. What we will record is another function, let us say $G(x_i, y_i)$, in the image plane represented by the subindex “i”. In general, we can write:

$$G(x_i, y_i) = \int_{-\infty}^{+\infty} \int_{-\infty}^{+\infty} H(x_i, y_i; x_0, y_0) I(x_0, y_0) dx_0 dy_0 \quad (\text{B.13})$$

The function $H(x_i, y_i; x_0, y_0)$ summarises all the defects and aberrations of our detection equipment, responsible for the imperfect reproduction of the image of the object. Usually, the acquisition process is supposed to be linear and invariant for translation, so that H has the form:

$$H = H(x_i - x_0, y_i - y_0). \quad (\text{B.14})$$

¹⁰For X-rays generated by a LINAC, tungsten or tantalum is usually used (at least 10 cm thick).

In this case, equation (B.13) assumes the form:

$$G(x_i, y_i) = \int_{-\infty}^{+\infty} \int_{-\infty}^{+\infty} H(x_i - x_0, y_i - y_0) I(x_0, y_0) dx_0 dy_0 \quad (\text{B.15})$$

The integral in the right hand side of equation (B.15) is the convolution of the function $I(x_0, y_0)$ with the function $H(x_i - x_0, y_i - y_0)$, so that one can formally write:

$$G = I * H \quad (\text{B.16})$$

Now consider the normalised Fourier transform of either $I(x_0, y_0)$ or $G(x_i, y_i)$ defined as:

$$I(\omega_x, \omega_y) = \frac{\int_{-\infty}^{+\infty} \int_{-\infty}^{+\infty} I(x_0, y_0) \exp\{-i(\omega_x x_0 + \omega_y y_0)\} dx_0 dy_0}{\int_{-\infty}^{+\infty} \int_{-\infty}^{+\infty} I(x_0, y_0) dx_0 dy_0} \quad (\text{B.17})$$

$$G(\omega_x, \omega_y) = \frac{\int_{-\infty}^{+\infty} \int_{-\infty}^{+\infty} G(x_i, y_i) \exp\{-i(\omega_x x_i + \omega_y y_i)\} dx_i dy_i}{\int_{-\infty}^{+\infty} \int_{-\infty}^{+\infty} G(x_i, y_i) dx_i dy_i} \quad (\text{B.18})$$

Remembering the convolution theorem, one gets:

$$G(\omega_x, \omega_y) = I(\omega_x, \omega_y) \cdot H(\omega_x, \omega_y), \quad (\text{B.19})$$

where

$$H(\omega_x, \omega_y) = \frac{\int_{-\infty}^{+\infty} \int_{-\infty}^{+\infty} H(x, y) \exp\{-i(\omega_x x + \omega_y y)\} dx dy}{\int_{-\infty}^{+\infty} \int_{-\infty}^{+\infty} H(x, y) dx dy}. \quad (\text{B.20})$$

H is known as the Optical Transfer Function (OTF) and is a complex function.

The absolute value of the OTF, $|H|$, is called as the Modulation Transfer Function (MTF) of the optical system. As the Fourier Transform of a Gaussian function is also a

Gaussian function, the MTF also usually has a Gaussian shape. The variables of the MTF are the spatial frequencies (usually in lp/mm) along two perpendicular directions and are directly related with the spatial resolution of the system. In practice, MTF gives fraction of the amplitude of a modulated signal, ranging from 100 to 0%, as a function of spatial frequency. Obviously, higher the frequency the worse the signal reproduction is. On the Internet, one can find instructive examples of MTF. For instance, in Ref. [48], it is possible to see the representation of MTF when a “bar pattern” and a “sine pattern” are reproduced by an optical system (film + lens).

APPENDIX C: CHARACTERISTICS OF SOME DETECTION SYSTEMS

C.1. General considerations

Many systems are used in digital imaging. In the text, we stated that there are two commonly used categories: “flat panels” and CCD + lens + scintillator systems. We will give an overview of the flat panels currently (mid-2004) available on the market and a guideline to choosing CCD system components suitable for diagnostic applications in cultural heritage. As this field is growing fast, we do not aim to provide complete information but merely give suggestions of how to tackle the question and how to plan searches on the Internet.

C.2. Flat panels

Flat panel digital detectors were introduced in the late 1990s as an alternative technology to traditional film, computed radiography and image intensifiers for medical imaging. These devices incorporate an X-ray detector and an integral sensor in a relatively compact design, hence the name flat panel. The detector is either an X-ray photoconductor or a scintillator, and the sensor is an amorphous silicon (a-Si) thin film transistor (TFT) array. Commercially available detectors use CsI or GOS scintillators coupled to an amorphous silicon TFT or to a CMOS photodiode array. Flat panels can basically be divided onto two types: direct and indirect. Both types are based on thin layers of a-Si deposited onto the glass substrates, with arrays of detector elements fabricated on the a-Si. For indirect conversion, the X-rays are first converted into visible photons, and then these photons are converted into electric charge. The scintillator, which converts X-rays to visible photons, is either grown directly on or attached to the TFT panel. For direct conversion flat panels, a different approach has been chosen: here the X-rays are directly converted into electric charges, which are then collected by the TFT array. Materials for direct conversion flat panels include amorphous selenium (a-Se), cadmium telluride (CdTe) and mercuric iodide (HgI_2).

As the performance of flat panels has improved and their cost has decreased, they have begun to challenge conventional imaging techniques, both in medical imaging and in other areas, such as industrial inspection and neutron imaging. These systems potentially offer a number of advantages over existing detector technologies, such as very compact size, large sensitive areas, and improved image quality under a wide range of imaging conditions. Flat panels offer substantial benefits for many X-ray imaging applications, in terms of resolution

Table C.1. Characteristics of some flat panels of a-Si + scintillator

Manufacturer – Model	Varian – PAXSCAN 4030R	General Electric – RADView Si40	Thales – FlashScan	PerkinElmer – RID1640
Total area	28 × 40 cm	28 × 40 cm	29 × 40 cm	40 × 40 cm
Scintillator screen	GOS	GOS	GOS	GOS (standard) or CsI (optional)
Pixel number	2304 × 3200	2304 × 3200	2240 × 3200	1024 × 1024 / 2048 × 2048
Pixel size	127 μm	127 μm	127 μm	400–200 μm
Output	12 bit	12 bit	14 bit	16 bit
Time/frame	~5 s	3.4 s	1.4 s	0.3 s

and dynamic range. In addition, they are physically robust and have good performance in terms of low noise and short readout time.

Commercial flat panels available on the market have a sensitive area up to 40 × 40 cm, with pixel size in the range between 50 and 400 μm. The output signal is usually 12 or 16 bit, and the number of pixels is comprised between 1×10^6 and 6×10^6 . The main applications are in medical imaging, where the voltage used is below 150 kV. However, flat panels could also be used, with proper adjustment, in high energy X-ray imaging and neutron imaging. Table C.1 contains the characteristics of some a-Si flat panels suitable for medium-high energy X-ray imaging.

C.3. CCD-based systems

The detection system described herein was developed by the Department of Physics of the University of Bologna for an important cultural heritage conservation institute. It is used mainly for diagnostics applied to ancient objects of archaeological interest and consists of several separate elements (see Fig. C.1):

- a metallic box with an internal guide for the movement of the CCD camera appropriately shielded by lead;
- a scintillating screen on which the X-ray beam generates the image;
- a mirror, angled at 45°, which reflects the image towards the camera;
- the CCD camera;
- a collimator, located in front of the screen, which decreases the radiation diffused by the object (sometimes the most important cause of image degradation);
- a pre-collimator, placed close to the X-ray source, which moulds the beam.

Each component must be chosen bearing in mind the energy range of the X-rays. DR and CT of objects of interest in the cultural heritage field are usually performed using

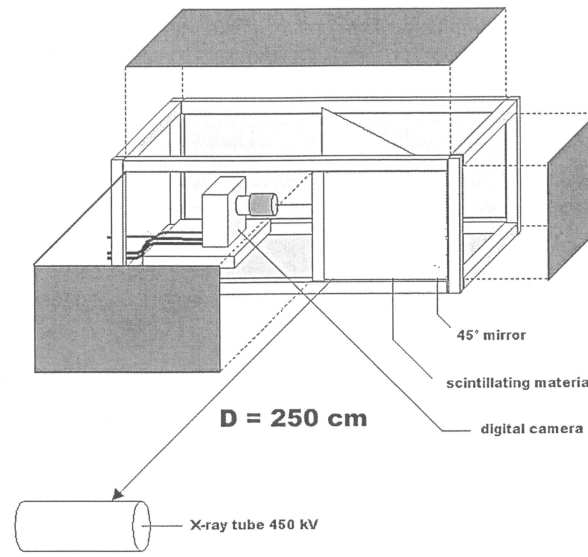


Fig. C.1. Detection system composed by scintillator screen + mirror + lens + CCD camera. Lead sheets protect the camera from scattered photons.

450 kV X-ray tubes or by 9 MeV LINAC. For X-ray tubes, the Pb should be at least 30 mm thick for both collimators and camera shielding. When using LINAC, the Pb should be at least 100 mm thick. Moreover, a sheet of lead glass must be placed in front of the camera to shield the photons that could reach the CCD sensor through the lens.

Scintillating screen

This is an extremely important component and should have the following properties:

- high light output per unit of energy dissipated within it (light photons released per MeV);
- low afterglow;
- high stability (chemical, temperature, hygroscopicity and radiation damage);
- high absorbing coefficient for X-ray photons;
- high MTF (good spatial resolution);
- emission wavelength well-matched to CCD sensitivity curve;
- not excessively expensive when used on large areas (*e.g.* 30 × 40 cm²).

A new material that satisfies all these requirements is caesium iodide (CsI) that is “structured” to form needles (Hamamatsu).

Another good scintillator is gadolinium oxysulfide (named GOS), which is cheaper than CsI. It can be smeared on a heavy metal sheet; so that light can also be produced by the

Table C.2. Principal characteristics of some scintillator materials

Scintillator	ρ [g/cm ³]	Refractive index n	Peak emission [nm]	Decay time [μs]	Light output [ph/MeV]	Radiation hardness [Gy]	Hygroscopic/ mechanical treatment
CsI (Na)	4.51	1.84	420	0.63	38500	<10 ⁶	yes/good
CsI (Tl)	4.51	1.80	550	0.9	59000	<10 ⁶	slightly/good
Nal (Tl)	3.67	1.85	415	0.23	38000	10 ²	yes/good
BGO (Bi ₄ Ge ₃ O ₁₂)	7.13	2.15	480	0.3	8000	10 ⁵	no/very good
GSO (Gd ₂ SiO ₅)	6.71	1.9	440	0.06	8000	>10 ⁸	no/bad
GOS (Gd ₂ O ₂ S)	7.34	2.2	510	3			no/good
CWO (CdWO ₄)	7.9	2.25	470	20	14000	10 ⁶	no/bad
LSO (Lu ₂ SiO ₅)	7.4	1.82	420	0.04	25000	>10 ⁷	no/acceptable
GSI glass	2.64	1.58	395	0.055	4000	10 ⁵	no/good
TB2 glass	2.64	1.58	550	3.5	6000	$\approx 10^6$	no/good
(Y,Gd) ₂ O ₃ :Eu	5.9	611	1000	1000	19000	21000	
Gd ₂ O ₂ S:Pr	7.3	513	3				

photo-electrons extracted from the metal layer, which dissipate their energy in the GOS. The LSF of CsI in needles is sharper than that of GOS.

Fiber-optic scintillator (FOS) are often used to obtain high spatial resolution. This scintillator is made with a plate of scintillating optical fibres sometimes covered by Lanex (another GOS-based material) (Kodak). The core of the scintillating fibre is made of heavy terbium activated glass.

In recent times, new matrix scintillators have been put in the market. These include the LSO (Lutetium oxyorthosilicate ($\text{Lu}_2\text{SiO}_5:\text{Ce}$)) and BGO (Bismuth Germanate ($\text{Bi}_4\text{Ge}_3\text{O}_{12}$)) models. Previously, these two scintillators were commonly used as single crystals but not as a matrix. The main characteristics of some scintillating materials are reported in Table C.2.

CCD camera

The camera, coupled with a lens, focuses the light emitted from the scintillating screen on the CCD chip and captures the image. The light emitted from the screen is reflected to the camera by a mirror. The mirror used must have high reflectivity (>95%) for the wavelength of the light emitted by the scintillator screen and no residual activation. Moreover, the wavelength of the light emitted by the screen must be in the range where the CCD has greatest sensitivity, usually around 550–600 nm (see Fig. C.2).

The digital camera is connected to a computer to upload the captured images stored in its memory. The PC interface could be a digital frame grabber or a standard PC connection (USB or Ethernet).

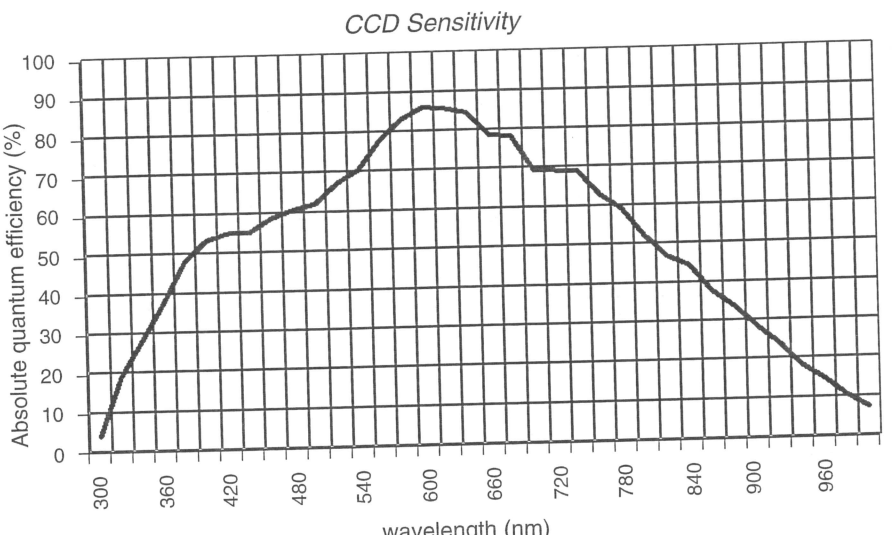


Fig. C.2. Efficiency of a CCD as a function of the wavelength (courtesy Apogee Instruments INC)

A CCD camera for digital imaging applications must have low noise and high efficiency. Depending on the budget available and on the parameters of the CT scans to be performed, one may choose one of several CCD sensors with different numbers of pixels, bits, pixel-sizes, quantum efficiencies, wavelength sensitivities and so on. As tomographic analysis requires a large number of good quality images (up to 1000), the read-out time for each frame is a very important parameter.

If only a little light is produced in the scintillator or if one wishes to acquire the images in a short time, an intensified camera (*i.e.* the Electron Bombarded CCD) can be used. Conversely, this kind of detector is affected by a greater electronic noise. In order to decrease the noise level or, better still, to suppress the dark current, CCD cameras have excellent cooling systems that can keep chip temperature at about 50°C lower than room temperature (~130°C with nitrogen).

In most cases, CCD cameras need to be coupled with a lens to focus the image on the chip and therefore the high brightness of the lens is very important in decreasing the exposure time. The larger the aperture of the lens, the greater is the difficulty in focusing the camera. In such cases, a micrometric stage is required. The best approach is to perform this operation directly from the control room of the bunker, on the radiographic image produced by X-rays on the scintillating screen. The picture distortion due to the lens (barrel or pin-cushion) can be corrected using software.

Otherwise, a CCD camera can acquire images without the lens by being coupled directly with a fibre optic plate or taper. To avoid image resolution loss, bond joints on CCDs must be perfectly matched. Moreover, in order to improve resolution and decrease cross-talk, one may choose from different kinds of fibre arranged in different configurations. Fibre optic bundles with individual fibre diameters as small as 3 microns can be bonded to CCD.

ACKNOWLEDGEMENTS

Much of the work described in this chapter was initiated by Massimo Rossi, a young researcher who tragically died from a terrible illness a few years ago, at the age of 35. This work is dedicated to him. The author wishes to thank all his young contributors, pictured in Fig. 69 (From right to left, they are: (stand up) Alessandro Pasini, Nico Lanconelli, Matteo Bettuzzi, Samantha Cornacchia, Maria Pia Morigi, Marilisa Giordano, Alice Miceli, the author; (sit down) Alessandro Fabbri, Davide Bianconi, Carlotta Cucchi, Emilia di Nicola. Not in picture: Davide Romani, Alberto Rossi, Rossella Brancaccio), for their enthusiasm in applying advanced techniques in the interest of the conservation and understanding important cultural treasures. Heartfelt thanks to Serena Pini (Musei Comunali, Florence) and to Giacomo Chiari, Senior Scientist of the Getty Conservation Institute, for their much appreciated collaboration.

REFERENCES

- [1] Y.V. Kuzumin, V.K. Popov, M.D. Glascock, M.S., Shackley, Sources of archaeological volcanic glass in the primorye (Maritime) province, Russian Far East, *Archaeometry*, **44** (2002), 505–515.
- [2] C.C. Graham, M.D. Glascock, J.R. Vogt, T.G. Spalding, Determination of elements in the National Bureau of Standards' geological standard reference materials by neutron activation analysis, *Analytical Chemistry*, **54**, (1982), 1623–1627.

- [3] W. Kockelman, Principles and Applications of Time-of-Flight Neutron Diffraction (TOF-ND) for Characterising Archaeological Ceramics and metal Artefacts. <http://www.ifac.cnr.it/corsoArcheo/abstract/Kockelmann.pdf>
- [4] *Radiation Protection Design Guidelines for 0.1–100 MeV Particle Accelerator Facilities*, NCRP Report No. 51.
- [5] VARIAN-1, <http://www.varian.com/sein/lm000.html>
- [6] Sincrotrone ELETTRA, Trieste, Italy, <http://www.elettra.trieste.it/info/index.html>
- [7] European Synchrotron Radiation Facility (ESRF), Seeing Things in a Different Light, <http://www.esrf.fr/info/>
- [8] M. Pantos, Synchrotron radiation in archeological and cultural heritage sciences, in: *4th Symposium on Archaeometry*, Athens, 2003.
- [9] S. Bracci, F. Falletti, M. Matteini, R. Scopigno, *Exploring David*, Ediz. Giunti Firenze Musei, pp. 221–226, 2004.
- [10] B. Illerhaus, J. Goebels, H. Riesemeier, *3D Computerized Tomography – Synergism Between Technique and Art*, <http://www.ct.bam.de/daten/paper.html>
- [11] H.E. Martz Jr., C.M. Logan, P.J. Shull, Radiology, in: P.J. Shull (Ed.), *Nondestructive Evaluation – Theory, Techniques, and Applications* (ISBN: 0824788729), The Pennsylvania State University, 2002.
- [12] NDT Resource Center, http://www.ndt-ed.org/index_flash.htm
- [13] R.E. Woods, R.C. Gonzalez, Real-Time Digital Image Enhancement, in: *Proceedings of the IEEE*, **69** (1981) 5, 643–657.
- [14] S. Di Zenzo, Advances in Image Segmentation, *Image and Vision Computing*, **1** (1983) 2, 196–210.
- [15] M. Rossi, F. Casali, P. Chirco, M.P. Morigi, E. Nava, E. Querzola, M. Zanarini, X-ray 3D computed tomography of bronze archaeological samples, *IEEE Transactions on Nuclear Science*, **46** (1999), 897–903.
- [16] H.C. Andrews, B.R. Hunt, *Digital Image Restoration*, Prentice-Hall, Englewood Cliff, New Jersey, 1977.
- [17] R.C. Gonzalez, P. Wintz, *Digital Image Processing*, Addison Wesley, Massachusetts, 1977.
- [18] R.C. Gonzalez, R.E. Woods, *Digital Image Processing*, second Ed., Prentice Hall, New Jersey, 2002.
- [19] W.K. Pratt (Ed.), *Digital Image Processing*, Strandberg, Denmark, 1985.
- [20] A. Rosenfeld, A.C. Kak, *Digital Picture Processing*, Academic Press, New York, 1976.
- [21] E.O. Brigham, *The Fast Fourier Transform*, Prentice-Hall, Englewood Cliffs, New Jersey, 1988.
- [22] V. Cappellini, *Digital filters and their applications*, Academic Press, 1981.
- [23] M. Rossi, F. Casali, S.V. Golovkin, V.N. Govorun, Digital radiography using an EBCCD-based imaging device, *Applied Radiation and Isotopes*, **53** (2000), 699–709.
- [24] Varian Paxscan 2020, <http://www.varian.com/xray/pdf/paxscan2020.pdf>
- [25] AETNA, <http://www.aetna.com/cpb/data/CPBA0380.html>
- [26] M. Bettuzzi, A. Pasini, A. Rossi, D. Schneberk, private communication, October 2004.
- [27] P. Von der Hardt, H. Rottger (Ed.), *Neutron Radiography Handbook*, D. Reidel Publishing Company, 1981. Revised by E. Heiberg, *Neutron Radiography. International Advances in NDT*. Vol. **16**, 1991.
- [28] Applied Science, www.appscientechn.com
- [29] R. Massari, R. Rosa, Neutron Tomography at the TRIGA reactor of ENEA, <http://info.casaccia.enea.it/triga/TRITON/>.
- [30] Doyle Group Harvard, <http://www.doylegroup.harvard.edu/neutron/publications/Theses/Park.pdf>
- [31] Imatron CT, <http://www.vaytek.com/heart1.htm>
- [32] A.C. Kak, M. Slaney, *Principles of Computerized Tomographic Imaging*, The Institute of Electric and Electronics Engineers, Inc., New York, NY, IEEE Press, 1988, Sec 6.4.1.
- [33] M. Bettuzzi, F. Casali, S. Cornacchia, M. Rossi, E. Paltrinieri, M.P. Morigi, R. Brancaccio, D. Romani, A new linear array detector for high resolution and low dose digital radiography, in: Proceedings IRRMA-V conference, Bologna, June 9–14, 2002, *Nuclear Instruments and Methods in Physics Research B*, **213** (2004), 227–230.
- [34] ARACOR, <http://www.aracor.com/pages/rocketmotor.html>
- [35] Bio-Imaging, <http://www.bio-imaging.com/detectors.asp>
- [36] General Electric High Speed CT, <http://www.bmimed.com/medical-imaging-products.asp>
- [37] L.A. Feldkamp, L.C. Davis, J.W. Kress, Practical cone-beam algorithm, *Journal of the Optical Society of America*, **1**(A) (1984), 612–619.
- [38] M. Rossi, F. Casali, M. Bettuzzi, M.P. Morigi, D. Romani, S.V. Golovkin, V.N. Govorun, An experimental micro-CT system for X-ray NDT, *SPIE Proceedings*, **4503** (2002), 338.
- [39] M. Rossi, F. Casali, D. Romani, L. Bondioli, R. Macchiarelli, L. Rook, MicroCT Scan in paleobiology: application to the study of dental tissues, *Nuclear Instruments and Methods in Physics Research B*, **213** (2004), 747–750.

- [40] A. Pasini, F. Baruffaldi, M. Bettuzzi, R. Brancaccio, F. Casali, S. Cornacchia, N. Lanconelli, M.P. Morigi, E. Di Nicola, S. Pani, E. Perilli, D. Romani, A. Rossi, A CCD-based high resolution CT system for analysis of trabecular bone tissue, in: *IEEE Medical Imaging Conference*, Rome, October 16–22, 2004.
- [41] Hitachi Heavy Industry, *Industrial X-ray CT for Digital Engineering*, <http://www.hitachi.com>
- [42] Paul Scherrer Institute, Neutron tomography <http://neutra.web.psi.ch/What/tomo.html>
- [43] T. Nakano, Y. Kawabata, M. Hino, U. Matsushima, Development of CT imaging system with very low energy neutrons, http://www.ttp.net/abstract_OR_prevauth.htm, 2004.
- [44] El-Bakkoush (2000), <http://www.ndt.net/article/wcndt00/papers/ldn704/ldn704.htm>
- [45] Filippo Giovanelli, *Tecniche di analisi non distruttive nello studio e nella tutela del patrimonio artistico*, Thesis, Università degli studi di Roma “La Sapienza”, Dipartimento di Ingegneria Nucleare e conversioni di energia, 2000/2001.
- [46] E. Deschler-Erb, E.H. Lehmann, L. Pernet, P. Vontobel, S. Hartmann, The complementary use of neutrons and X-rays for non-destructive investigation of archaeological objects from Swiss collections, *Archaeometry*, **46** (2004) 4, 647.
- [47] A.A. Harms, D.R. Wyman, *Mathematics and Physics of Neutron Radiography* (ISBN: 9027721912), Kluwer Academic Publishers, The Netherlands, 1986.
- [48] H. Fujita et al., A simple method for determining the Modulation Transfer Function in digital radiography, *IEEE Transactions on Medical Imaging*, **11**, No. 1, March 2000.
- [49] N. Koren, <http://www.normankoren.com/Tutorials/MTF.html>
- [50] J.H. Hubbell, S.M. Seltzer, Tables of mass attenuation coefficients for X-rays, <http://physics.nist.gov/PhysRefData/XrayMassCoef/cover.html>